Democratic and Popular Republic of Algeria

Ministry of Higher Education and Scientific Research

Chadli Bendjedid University – El Tarf

Faculty of Sciences and Technology

Process Engineering Department

Professional Master's Thesis

Field: Sciences and Technology

Major: Process Engineering

Specialty: Water Treatment and Desalination

Theme:

Synthesis, Characterization and Photocatalytic application of LDO-Based Catalysts for the degradation of Organic Pollutants in Aqueous Medium.

Presented by :

Ms. DIABI Nour El Imane

Defended on June 18th, 2026 before the jury

Dr OTMANI Lhadi	**President**	**MCB**	**Univ. El-Tarf**
Dr BELAIDI Ouafa	**Examiner**	**MCB**	**Univ. El-Tarf**
Dr BENIDIR Sofiane	**Supervisor**	**MCB**	**Univ. El-Tarf**
Dr SMILI Billel	**Co-Supervisor**	**MCA**	**Univ. El-Tarf**

Academic Year : 2025/2026

AT THE HEART OF EVERY DISCOVERY LIES A QUESTION

"The important thing is not to stop questioning. Curiosity has its own reason for existing."

— ALBERT EINSTEIN

DEDICATION

.

To my lovely mommy" NAZIHA", I am deeply grateful for your endless love, sacrifices, and constant support, which have been my greatest source of strength and inspiration.

To my father" NACER", I sincerely thank you for your hard work, guidance, and unwavering dedication to our family, which has always motivated me to move forward.

To RIHAB, HASNA, IBRAHIM, and ARSLEN for being my greatest source of love, support, and happiness.

last but not least I want to thank me, I want to thank me for believing in me, I want to thank me for doing all this hard work, I want thank me for having no days off, I want to thank me for just being me at all times.

✦ ✦ ✦

ACKNOWLEDGMENTS

Before all else, I thank God for every blessing, every opportunity, and every challenge that contributed to my growth and enabled me to reach this important milestone.

I would like to express my profound gratitude to ***Dr. BENIDIR SOFIANE****, for his valuable guidance, scientific expertise, and constructive suggestions throughout the course of this work. His support and insightful comments have played a significant role in shaping this research.*

I extend my highest appreciation to ***Dr. SMILI BILLEL*** *for his assistance, insightful recommendations, and continuous encouragement. His contributions have greatly enhanced the quality and development of this study.*

I would also like to warmly thank ***Dr. OTMANI LHADI****, who always believed in my abilities and encouraged me to persevere, even in moments of doubt. Their words of encouragement had a defining influence on my journey.*

My special thanks are extended to ***Dr. BELAIDI OUAFA****,* ***Dr. BEKAKRIA HAMIDA****, and* ***Dr. SAAIDIA SAMIA*** *for their support and assistance throughout the laboratory work. I am particularly grateful for their guidance, constructive advice, and readiness to share their knowledge and expertise whenever needed.*

Furthermore, I would like to express my gratitude to the members of the jury. I would like to extend my gratitude to ***Dr. OTMANI LHADI*** *for agreeing to chair this jury and to* ***Dr. BELAIDI OUAFA*** *for agreeing to examine this work. I would like to express my gratitude to all those who have participated in this experience.*

✦ ✦ ✦

List of abbreviations

AOPs	Advanced oxidation processes
CB	Conduction band
CR	Congo Red
DSC	Differential scanning calorimetric
ECs	Emergent contaminants
Fe	Iron
FTIR	Fourier Transform Infrared Spectroscopy
HCl	Hydrochloric acid
ICTA	International Confederation for Thermal Analysis
LDHs	Layered double hydroxides
LDOs	Layered double oxides
MOs	Metal oxides
Ni	Nickel
NPs	Nanoparticles
PCPs	Personal care products
PFAS	Per- and polyfluoroalkyl substances
STA	Simultaneous thermal analysis
TGA	Thermogravimetric analysis
VB	Valence band
XRD	X-ray diffraction
Zn	Zinc
Λ_{max}	Wavelength of Maximum Absorbance

Table of Contents

Chapter III : Results and Discussion

List of Figures

Chapter I

Chapter II

Chapter III

List of Tables

Chapter I

Chapter II

Chapter III

General introduction

General Introduction

Due to the steady increase in population, along with rapid industrial and agricultural expansion, access to clean, potable water sources have become more and more difficult, this has led to the discharge of a wide variety of non-biodegradable, hazardous organic contaminants, including dyes, pharmaceuticals, and pesticides, into aquatic system. When their persistence poses significant threats to aquatic biota, human health, and overall environmental sustainability **[1].**

Conventional water treatment processes often fail to completely degrade these pollutants owing to their complex chemical structures and high stability, which highlights the urgent need for advanced and sustainable treatment technologies to achieve high removal efficiencies. Consequently, advanced oxidation processes and other non-conventional approaches have gained considerable attention recently, as effective solutions for water pollution control. In this context, layered double hydroxides based materials have emerged as promising multifunctional systems combining excellent adsorption capacity with photocatalytic activity, due to their unique thermal decomposition, memory properties, tunable interlayer metal cations**,** and their ability to modify the band gap **[2,3].**

This present work is organized into three chapters:

The first chapter I provides a theoretical review of the current state of water pollution with different organic pollutants and their associated environmental impact, it also examines the conventional and non-conventional water treatment technologies including the advanced oxidation processes (**AOPs**), nanotechnology, and nanoparticles. With a particular emphasis on the layered double hydroxides (**LDHs**) and layered double oxides (**LDOs**), their structure, synthesis methods, and application in photocatalysis and adsorption processes. With special focus on **NiZnFe-based LDO**.

The second chapter II describes the materials, synthesis procedures, and characterization techniques employed for the preparation of the LDO-based catalyst, additionally it provides an overview on the anionic dye Congo Red (**CR**) selected as the target organic pollutant, for evaluating the behaviour of the synthesized material as both an adsorbent and a photocatalyst.

The third chapter presents the characterization techniques, including UV-Vis spectrometry, X-rays diffraction (**XRD**), three-dimensional profilometry, Fourier-Transform InfraRed (**FTIR**) spectroscopy, and simultaneous thermogravimetric analysis (**TGA/DSC**) employed to investigate the structural, morphological, optical, and physicochemical properties of the synthesized NiZnFe-based LDO, It also discusses the adsorption process, including the experimental methodology, adsorption performance, and the factors influencing the removal of organic dye CR from aqueous media.

References

[1]- Bashir, I., Bhat, R. A., Mir, S., & Dar, Z. (2020). Chapter 1: concerns and threats of contamination on aquatic ecosystems in: bioremediation and biotechnology. University of agricultural sciences and technology, Jammu, Jammu and Kashmir, India. Bioremediation and biotechnology: sustainable approaches to pollution degradation, 1–26.

[2]- Luo, L., Hou, C., Wang, L., Zhang, W., Wang, C., Liu, J., ... & Wang, C. (2024). Layered double hydroxide-based photocatalysts for the removal of emerging contaminants: progress in past ten years. *Catalysts*, *14*(4), 252.

[3]- Imran, S., Hussain, M. (2025). Layered double hydroxide-based photocatalysts for hydrogen production: Innovations, attributes and future prospects. *International Journal of Hydrogen Energy*, *127*, 311-330.

Chapter I :

Aquatic pollution &

remediation technologies

Chapter I : Aquatic pollution & remediation technologies

I.1 General Intro to aqueous pollution

While chemical substances have undeniably improved our lives, they come with a serious downside; they can be harmful to both human health and the environment. Years of uncontrolled and poorly regulated use of man-made chemicals have pushed humanity past the safe limits our planet can tolerate **[1].** Aquatic pollution stands at the forefront of both scientific and public concern, as ecosystems face mounting pressure from a diverse array of chemical substances originating from agricultural, industrial, and domestic activities. Although beneficial to human well-being but their overuse still represents one of the pressing challenges nowadays threatening drinking water security **[2].**

Contaminants such as: Pesticides, heavy metals, polycyclic aromatic hydrocarbons and more, recently microplastic particles, pharmaceuticals, and dyes are continuously introduced into water bodies as a result of anthropogenic activities. Their presence raises serious alarms regarding the health of plants, animals, and humans alike, owing to their acute toxicity and the risk of accumulating within living organisms **[3].**

I.1.1 Organic pollutants

Besides the previously mentioned contaminants, emerging pollutants encompass a wide variety of compounds including personal care products (**PCP**s), organic dyes, per- and polyfluoroalkyl substances (**PFAS**), micro- and nano-plastics **(MNPs).** The presence of these ECs across various environmental matrices has grown steadily, driven by the relentless rise in human activities **[4]**, once released into the aquatic environment, these compounds exhibit persistent behavior, as many are resistant to natural biodegradation, and tend to accumulate in sediments and living organisms through bioaccumulation and biomagnification along the food chain **[5].**

I.1.2 Pharmaceutical products

Pharmaceuticals and PCPs have become an integral part of daily life providing substantial benefits to human health and well-being, medications ranging from antibiotics to antidepressants have become indispensable in modern healthcare, contributing greatly to improved life expectancy and enhanced quality of life **[6]**, Pharmaceuticals are known to be chemically stable active substances intended to trigger biological responses in target organisms **[7]**, yet they constitute a significant class of aquatic contaminants and can seriously threaten the health of non-target organisms **[2]**, through the discharge of raw, contaminated,

and inadequately treated pharmaceutical wastewater into water supplies and river channels that contribute to short, medium, and long- term environmental and human health impacts **[8,9]**.

As shown in the figure **(I.1)** these drugs impact growth, reproduction, development, physiology, behaviors, and mortality in coastal and marine organisms, the rise of antibiotic-resistant bacteria in marine ecosystems, combined with disrupted animal behavior and impaired reproductive patterns, has become a growing concern. On top of that, antihypertensive drugs, beta-blockers in particular, interfere with cardiovascular function in marine fish, slowing heart rate and disturbing blood pressure regulation **[6]**.

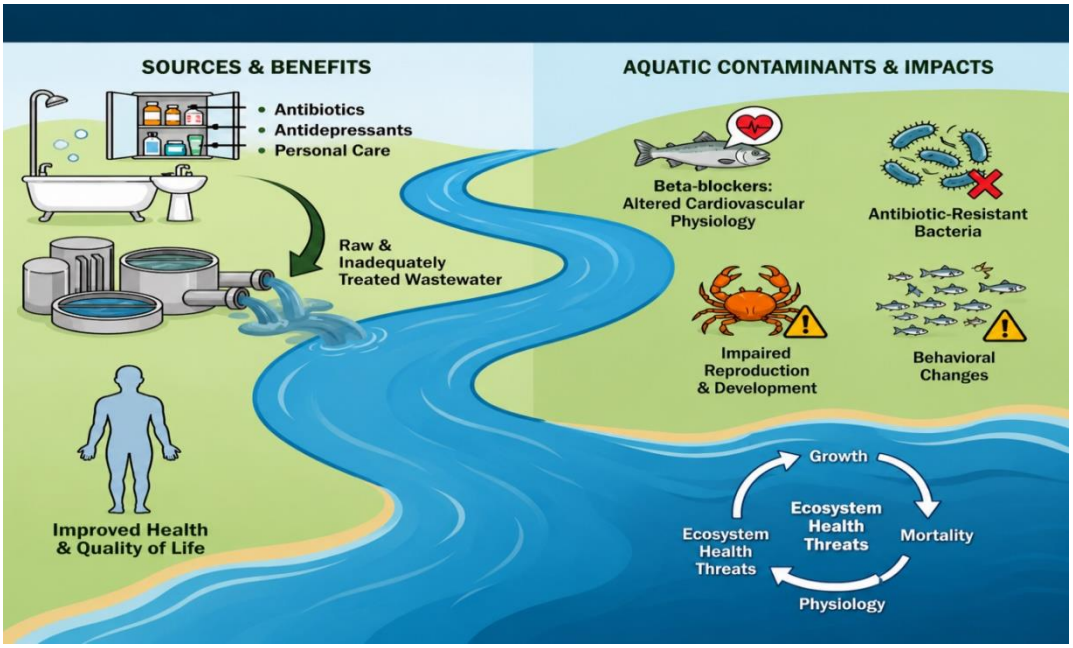

Fig.I.1. *Pathways and Environmental Consequences of Pharmaceutical Pollutants in Aquatic Systems (AI generated).*

Emerging pollutants also known as “emerging contaminants” ECs, are biological agents, organic or inorganic compounds of anthropogenic or natural origin, mostly found at trace concentrations ($ng.L^{-1}$ and $\mu g.L^{-1}$) in the environment **[9]**, also considered as ubiquitous, toxic and persistent in the environment, and represent long-term and unpredictable threats to human beings and ecosystem **[10]**.

I.1.3 Pesticides

Pesticides are chemicals deliberately introduced into the environment to eliminate specific pests, serving not only to control plant-based diseases but also to boost agricultural

output. Their consumption has grown steadily, driven by the increasing demand for food production and crop storage to meet the needs of a rising global population. Being synthetic in origin and highly stable, these compounds do not break down easily in the environment. Their inappropriate and unscientific use, poor handling, and careless disposal have allowed them to find their way into water bodies, causing serious damage to the ecosystem and the environment **[11]**.

Once in aquatic systems, pesticides pose a direct threat to non-target species, fish being among the most vulnerable where acute exposure has led to death while milder exposure has caused irreversible damage to vital organs such as the liver, kidneys, gills, and the brain. Beyond aquatic life, human exposure through contaminated water has been linked to a range of chronic diseases including cancer, diabetes, cardiac conditions, and neurobehavioral disorders **[12]**.

I.1.4 Synthetic Organic dyes

Dyes are complex unsaturated chemical compounds with the ability to absorb a portion of light in the visible range (**380-750 nm**). This absorption occurs through chromatophoric groups, specific clusters of atoms **[13]**, selectively absorb energy and change white light into colored light when it reflects off of a body or diffuses through the air, those groups are :

- **Chromophores (the color-bearing groups):** The active sites of the dyes that govern the spatial arrangement of light-absorbing atoms are unsaturated regions where single and double bonds alternate in a conjugated and resonant pattern, enabling the absorption of visible light. These regions typically contain heteroatoms such as N, O, and S and feature characteristic bonds including -N=N- (azo), =C=O (carbonyl), NO or N-OH (nitrous), -NO_2 or NO-OH (nitro) and C=S (sulfur) **[14, 15]**.
- **Auxochromes (the color helpers):** are functional groups that are not responsible for color but are for intensity (tone) and affinity for the fiber, some of them are-NH_3 (amine), -COOH (carboxyl), HSO_3 (sulphonate) and –OH (hydroxyl) **[14]**.

While their persistence and resistance to biodegradability under normal environmental conditions alter both the physical and biological characteristics of aquatic ecosystems, they interfere with photosynthesis in marine plants by triggering eutrophication through the uncontrolled discharge of mineral elements namely nitrates, nitrites and phosphates.

This disrupts the balance of the aquatic environment, giving rise to long-term hazards including mutagenicity, bioaccumulation, and carcinogenicity **[17]**.

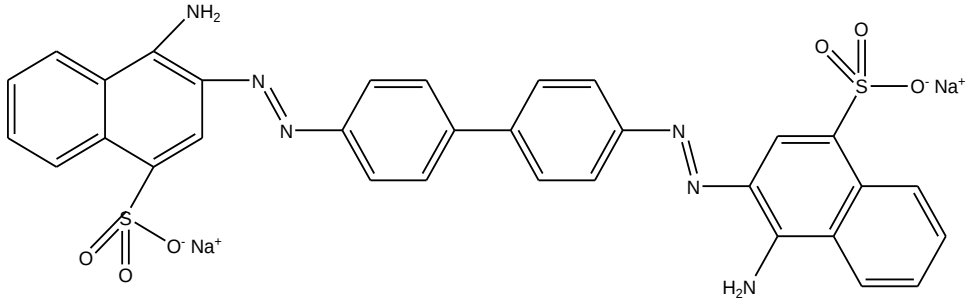

Chromophore (azo group –N=N–) Auxochrome (–NH_2)

Fig.I.2. *Chemical structure of Congo red highlighting its chromophore and auxochromic groups* ***[16]****.*

I.1.5 per- and polyfluoroalkyl substances

Per- and polyfluoroalkyl substances **(PFAS)** commonly referred to as "forever chemicals", are a group of synthetic compounds defined by an exceptionally stable hydrophobic carbon-fluorine (C–F) bond backbone **[18]**. This amphiphilic structure is responsible for their distinctive properties and has made them a worldwide environmental concern, due to their serious impacts on biological health. PFAS are widespread contaminants in aquatic ecosystems, exhibiting significant bioaccumulation and biomagnification across trophic levels, generating considerable ecotoxicological risks **[19]**, even at environmentally relevant concentrations, they are capable of triggering multiple toxic effects in organisms at different trophic levels, including potential carcinogenicity, reproductive developmental toxicity, immunosuppression, and endocrine disruption **[20]**.

These effects not only pose a direct threat to aquatic organisms, but may also pose a potential risk to human health through the food chain. Their persistence and mobility allow them to spread through water systems, and accumulate in aquatic organisms, making aquatic environments a major exposure route **[21]**.

I.2 Water treatment technologies

The growing burden of environmental contamination in aquatic ecosystems, spanning the pollution of aquifers and groundwater, affecting water quality, and increasing the risk of diseases **[22]**, has underscored the urgent need for reliable access to clean, safe water for public health, quality of life, and long-term environmental sustainability, in response to these

pressing challenges, a range of advanced and innovative water treatment technologies such as advanced oxidation processes **(AOPs)**, adsorption-based processes, and other physicochemical treatment methods, has emerged as essential solutions. The technologies to be chosen for each individual pollutant depend on the presence of other pollutants, their concentration, the quantity of water to be treated, and the intended use of the water **[23]**.

I.2.1 Conventional treatment approaches

Water treatment processes offer multiple effective mechanisms for pollutants removal in water treatment systems, and they can be integrated with other treatment methods. These techniques are broadly categorized into two types: conventional as shown in **Table I.1** and non-conventional approaches. Treating water traditionally goes through a few stages:

- **Preliminary treatment:** involves the initial removal of large solids and debris through screening and grit removal, to protect downstream equipment from damage and clogging.
- **Primary treatment:** then removes suspended solids and organic matter via sedimentation and flotation, reducing the organic load and turbidity of the wastewater for further processing.
- **Secondary treatment:** air is introduced through aeration to stimulate microbial activity (oxidation), which in turn facilitates the biodegradation of organic pollutants employing microorganisms, including activated sludge, trickling filters, and sequencing batch reactors.
- **Tertiary treatment:** purifies water quality through filtration, chemical treatment, and advanced biological processes. Disinfection is achieved using techniques such as chlorination, UV irradiation, and ozonation to eliminate residual pathogens, while sludge management through digestion, dewatering, and incineration ensures safe disposal or reuse of byproducts **[24,25]**.

These techniques often fall short for achieving higher treatment efficiency, which has driven the development of non-conventional approaches, among which photocatalysis and advanced adsorption processes have emerged as particularly promising methods **[22].**

Table I.2 : *Main conventional water treatment processes.*

Technology	Stage	Advantages	Limitations	Ref
Screening/ sedimentation	Primary	No chemical addition. Simple & low cost. Reduces load for next stages.	Cannot remove dissolved pollutants. Large sludge volume generated.	**[26]**
Biological treatment	Secondary	Environmentally friendly. Cost effective at scale. Removes organic load.	Slow biodegradation. Ineffective for refractory compounds.	**[27]**
Coagulation & flocculation	Tertiary	Widely established Effective turbidity removal. Simple operation.	Large sludge production. Poor removal of dissolved ions.	**[28]**

I.2.2 Non-conventional treatment approaches

The evolving range of contaminants in wastewater highlights the need for continuous innovation and the integration of advanced treatment methods. Prioritizing research and development in wastewater management is essential to overcome the limitations of conventional systems and maintain their effectiveness against emerging environmental concerns. Consequently, alternative methods that provide enhanced efficiency, cost-effectiveness, and environmental sustainability are increasingly sought after. Non-conventional water treatment approaches have therefore emerged as promising solutions, offering novel and effective strategies to address the complex nature of wastewater contamination **[25]**.

I.2.2.1 Nanoparticles

The British Standards Institution, proposed the following definitions; "Nanotechnology" as the manipulation and control of matter on the nanoscale dimension by using scientific knowledge of various industrial and biomedical applications, typically; within the range of one billion of a meter **1nm = 1*10^{-9} [29]**. "Nanoparticle" is a nano-object with three external nanoscale dimensions. When the longest and shortest axes of the nano-object have different lengths, the terms "nanorod" or "nanoplate" are used instead of nanoparticle

(NP), and "Nanostructure" which is the Composition of interconnected constituent parts in the nanoscale region.

NPs are broadly classified according to their composition into: Carbon-based, Inorganic-based, Organic-based, and Composite-based nanomaterials; among which inorganic-based materials particularly metal oxides and layered double hydroxides (LDH) have garnered growing research interest in water treatment applications owing to their tunable surface properties and high adsorption capacity **[30]**.

I.2.2.2 Photocatalysis as an AOP

Photocatalysis is a photochemical process within advanced oxidation processes AOPs. It is a light-induced oxidative reaction capable of degrading a wide variety of ECs in water, operating under mild conditions and compatible with solar energy. The photocatalytic reaction can occur in two ways: homogeneously or heterogeneously depending on the relationship between the photocatalyst (i.e. semiconducting material), and the reactant **[31]**.

- **Heterogeneous photocatalysis:** Refers to the process in which both the reactant and the photocatalyst are present in the same phase.
- **Homogeneous photocatalysis:** The reactant and photocatalyst are present in distinct phases **[32]**.

As shown in **Figure I.3** Upon light irradiation with photon energy equal to or greater than the band gap of the photocatalyst, electrons (e^-) in the valence band (VB) are excited to the conduction band (CB), leaving behind positively charged holes (h^+) in the VB.

The photo generated charge carriers subsequently migrate toward the catalyst surface, where they participate in redox reactions. Electrons (e^-) in the CB reduce molecular oxygen (O_2) to superoxide anions ($O_2\bullet^-$) while holes (h^+) in the VB oxidize hydroxide ions (OH^-) to generate hydroxyl radicals (•OH). The overall photocatalytic efficiency depends on the balance between light absorption, charge carrier separation, and interfacial redox dynamics **[33]**.

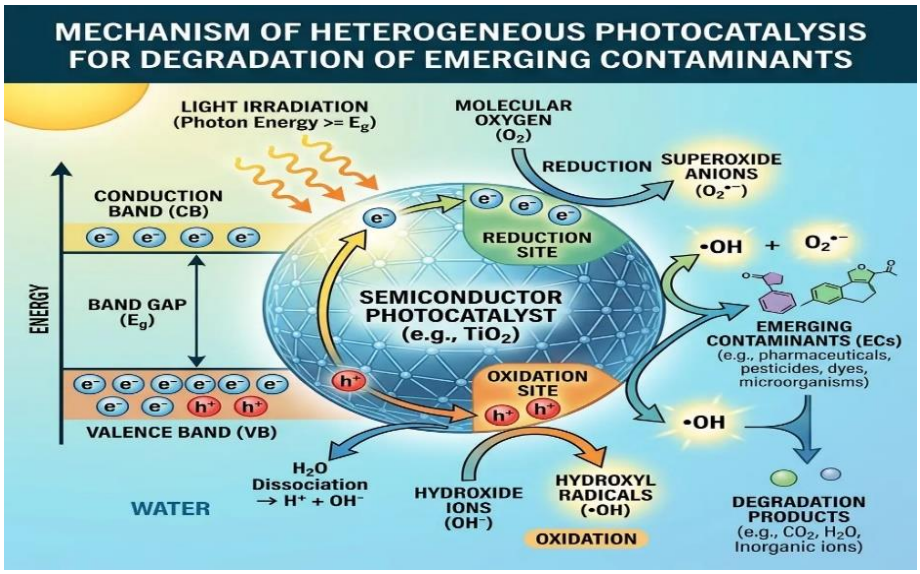

Fig.I.3. *Mechanism of heterogeneous photocatalysis for ECs degradation (AI generated).*

I.2.2.3 Photocatalysis using mixed oxides

Mixed oxides exhibit desirable properties, including high surface area, enhanced thermal and structural stability, and tunable composition and porosity **[34]**. Among their most notable properties is what commonly known as “memory effect”. This particular property allows MOs to recover their original LDHs structure under mild conditions (ambient temperature, atmospheric pressure) **[35]**, following upon prolonged exposure to aqueous solutions or air; this behavior introduces a distinctive approach to modifying LDH materials, as it preserves their original active sites while simultaneously increasing the number of accessible sites, thereby expanding their potential for applications in adsorption and catalytic processes.

However, it is very important to emphasize that the reconstruction of layered structure is possible only for certain calcination temperatures. When calcination temperatures exceed 600°C and spinel phase formation occurs, the memory effect will not take place or it will be insignificant **[36]**.

MOs have attracted considerable attention as promising nanomaterials, capable of acting both as independent absorbent and as key constituents in the fabrication of composite adsorbent systems, owing to their distinctive physicochemical properties **[37]**.

I.2.2.3.1 Layered Double Hydroxides

Layered double hydroxides **(LDHs)** , also known as anionic clays or hydrotalcites, are two-dimensional materials **(2D)** lamellar materials, the LDH structure consists of positively

charged brucite-like layers composed of metal hydroxide octahedral units, with anions and water molecules intercalated in the interlayer space, forming catalysts with enhanced properties, the general formula is as follows **[38]**;

$$[M^{II}_{1-x}M^{III}_{x}(OH)_2]^{x+}(A^{n-})_{x/n}$$

Where:

- M^{II} is a bivalent metal cation, such as Mg^{2+}, Zn^{2+} or Ni^{2+}.
- M^{III} is a trivalent metal, such as Al^{3+}, Ga^{3+}, Fe^{3+}.
- x is the mole ratio of $M^{III}/(M^{II} + M^{III})$, (normally between 0.17 and 0.33).

The **figure I.4,** shows their structure that resembles of brucite $[Mg(OH)_2]$, where Mg^{2+} ions form sheets of octahedral coordination stacked together through hydrogen bonding, Structural properties, surface area, interlayer anion exchange capacity, tunability, and memory effect of LDHs render them suitable for a broad range of applications.

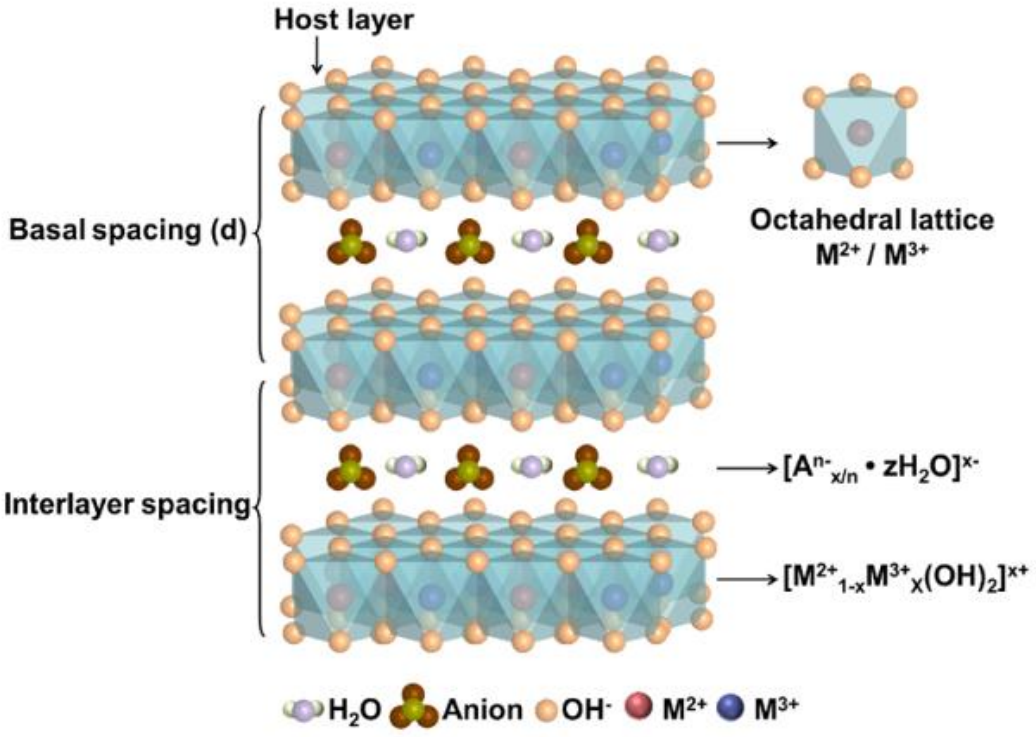

Fig.I.4. *Schematic view of the $M^{2+}M^{3+}$ LDH general structure* ***[39]***.

They can be created utilizing simple approaches that regulate the layer structure, chemical composition, and shape of the crystals generated by adapting production parameters, the most commonly used synthesis methods are summarized in the **table I.2.**

Table I.2 : *Comparative overview of LDH synthesis methods*.

Method	Principle	Morphology	Advantages	Ref
Co-precipitation	Alkaline medium ($NaOH/Na_2CO_3$); Simultaneous precipitation of metal salts.	Nanoparticles, Sheets. Irregular aggregates. Moderate crystallinity.	Simple and cost-effective. High purity and homogeneity. Large scale production.	**[40]** **[41]**
Sol gel	Poly-condensing a molecule precursor using liquid.	Porous nanostructures. Amorphous particles. Core-shell. High crystallinity.	High purity and uniformity. Efficient conducted at low temperature.	**[42]**
Urea hydrolysis	Using urea as the primary precipitating agent, inducing homogeneous precipitation of metal salts.	Porous platy & monodisperse particles. High crystallinity.	High purity. Better cyclic stability.	**[43]**
Hydrothermal	Crystallizing metal salt precursors under high temperature and autogenous pressure in a sealed aqueous medium.	Well-ordered nanoplates/ nanosheets High crystallinity.	Controlled morphology Tunable size/structure. Large surface area.	**[44]** **[43]**

I.2.2.3.2 Layered double oxides LDOs

Layered double oxides are synthesized through the calcination of LDHs, a thermally driven process that decompose the interlayer structure, ultimately yielding highly dispersed metal oxide phases **[45]**. This thermal treatment induces a structural transformation in the crystalline framework of LDH, transforming from an octahedral to a tetrahedral configuration, thereby facilitating the formation of mixed metal oxides **[46]**.

The process effectively generates an increased concentration of positively charged cations, with the crystalline structures developing compensating defects. These defects include the presence of oxygen and cationic vacancies, to produce the well-defined 3D framework of diverse metal oxides as shown in **Figure I.5** three systematic reactions occur

during the calcination of LDHs: the efficient removal of adsorbed and interlayer water molecules, followed by the controlled dihydroxylation of the layers, and finally the productive decomposition of the anions **[47]**.

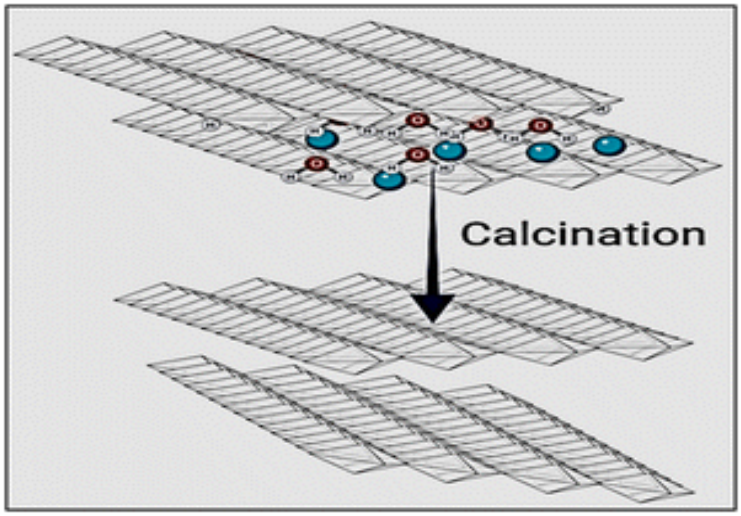

Fig.I.5. *Mixed metal oxide in a 3D LDH structure [47].*

I.2.2.3.2.1 Iron-based LDHs

Iron-based LDHs are considered as superior photocatalysts, due to their layered structure, compositional flexibility, and cost-effectiveness; Fe-based LDHs are characterized by easy production, low-cost growth, a high specific surface area, and a dense concentration of active centers that enhance their catalytic performance. Furthermore, their narrow bandgaps, make them ideal for photoelectrochemical applications under visible light **[48]**. **Table I.3** summarizes the key properties of Fe^{3+} in the LDH structure.

Table I.3 : *Properties of Iron (Fe) in LDHs* ***[50].***

Properties	Value/description
Oxidation state	Fe^{3+}(trivalent)
Bandgap	~2.2 eV (visible light absorption).
Redox couple	Fe^{3+}/Fe^{2+} (facilitates electron transfer).
Photocatalytic role	Generates $OH^-$and O_2^- radicals.
Advantages	Low cost, abundant, easy production.

I.2.2.3.2.2 Nickel-based LDHs

Nickel (Ni), the most active catalytic materials is widely exploited as a co-catalyst and to modify the electrode surfaces, in both electrocatalysis and photocatalysis respectively, Table I.4 summarizes the key properties of Ni^{2+} in the LDH structure **[50]**.

Table I.4 : *Properties of Nickel (Ni) in LDHs* ***[50].***

Properties	Value/description
Oxidation state	Ni^{2+}(divalent)
Bandgap	~4,47 eV
Redox couple	Ni^{2+}/Ni^{3+} (enhances charge transfer).
Photocatalytic role	Excellent inhibitor vanquishes the back reaction.
Advantages	Low cost, good conductivity, availability of abundant active sites.

I.2.2.3.2.3 Zinc-based LDHs

Zinc oxide (ZnO) is a low cost, abundant, biocompatible, wide-bandgap semiconductor with easily tunable morphologies and properties, making it one of the most studied metal oxides. Due to its versatility, straightforward bandgap engineering, with transition and rare-earth metals, and diverse nanomorphologies, ZnO serves as a promising photocatalyst **[51]**, **Table I.5** summarizes the key properties of Zn^{2+} in the LDH structure.

Table I.5 : *Properties of Zinc (Zn) in LDHs* ***[51].***

Properties	Value/description
Oxidation state	Zn^{2+}(divalent)
Bandgap	~ 2,5 eV
Redox couple	Redox inert
Photocatalytic role	High photostability, broad range of radiation absorption.
Advantages	Optical and electrical properties (transparency, electrical mobility)

I.3 Advanced adsorption process

Adsorption is a unit operation occurs through contact between a liquid phase containing one or more contaminants (adsorbate) to be removed, and a solid material (adsorbent), this process is driven by a surface imbalance whether attractive or repulsive, that pulls the contaminant toward the solid through physical or chemical interactions. This mass transfer continues until a balance is established between the contaminant retained on the solid and the amount remaining in the liquid phase, this is termed equilibrium **[52]**.

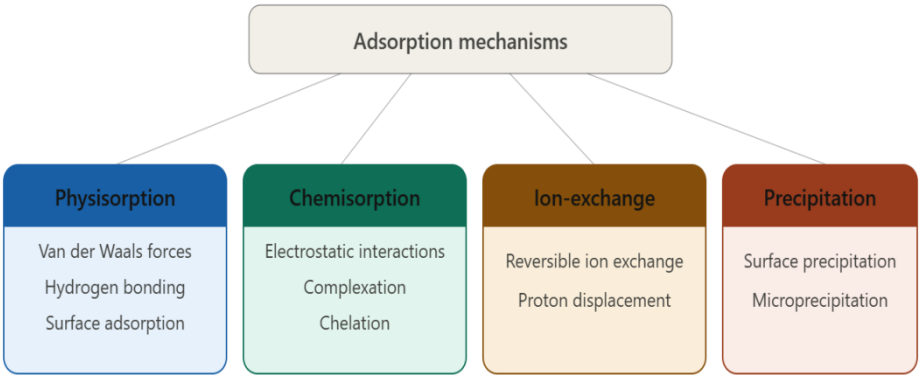

Fig.I.6. *Classification of adsorption mechanisms* ***[53].***

According to **Crini et al.(2019)**, in an adsorption process using a specific adsorbent, more than one of these mechanisms may occur simultaneously depending on the nature of the adsorbent, the properties of the contaminants, and the solution conditions such as pH, ionic strength, temperature **[53].**

I.3.1 Factors affecting the adsorption

The high anion exchange capacity and large surface area of LDHs, their flexible interlayer region that is accessible to various ionic and non-ionic compounds are important characteristics promising their better removal performance of contaminants from aqueous system **[54]**. However, the efficiency of the adsorption process is not governed only by the properties of the adsorbent, several operational and physicochemical parameters as shown in **Table I.6** significantly influence adsorption behavior and overall removal efficiency.

Table I.6 : *Operational Parameters Affecting Adsorption Efficiency **[55]**.*

Parameter	Influence on the Adsorption
pH	Controls the surface charge of the adsorbent and the speciation of pollutants in solution, affecting electrostatic interactions.
Contact Time	Determines the time required to reach adsorption equilibrium.
Initial Pollutant Concentration	Influences the adsorption capacity and the degree of active site saturation.
Adsorbent Dosage	Higher dosage increases the number of available active sites and the removal rate, but decreases the adsorption capacity per unit mass.
Temperature	Favors adsorption by increasing diffusion rate, reducing solution viscosity, and increasing surface area though some systems show exothermic behavior where adsorption decreases with temperature.

I.3.2 Adsorption isotherms

Adsorption isotherms describe the equilibrium distribution of the adsorbate molecules between the liquid phase and the adsorbent surface**.** In addition, isotherms help to provide information for evaluating adsorption performance and optimizing adsorbent utilization.

Among the various empirical models that have been used to describe how adsorbates interact with adsorbents, the Langmuir and Freundlich models are the most widely used for LDO-based adsorbents, in which The Langmuir model assumes monolayer adsorption on a homogeneous surface with identical adsorption sites, as described by **Eq (I.1)**, whereas the Freundlich model describes adsorption on heterogeneous surfaces and is particularly suitable for low adsorbate concentrations **Eq (I.2) [54]**.

$$q_e = (q_m K_L C_e) / (1 + K_L C_e) \qquad \textbf{Eq (I.1) [56]}$$

Where :

q_e = amount adsorbed at equilibrium (mg g^{-1})

q_m: maximum adsorption capacity (mg g^{-1})

C_e = equilibrium concentration (mg L^{-1})

K_L = Langmuir constant (L mg^{-1})

$$q_e = k_f C_e^{1/n} \qquad \textbf{Eq (I.2) [56]}$$

Where:

n: adsorption intensity parameter

I.4 Conclusion

LDHs exhibit excellent adsorption and photocatalytic properties; however several challenges still limit their widespread application **[54]**:

- The low mechanical resistance that may causes problem for continuous water treatment units and in certain regeneration processes, as LDHs can be exfoliated **[52].**
- Due to their small particle size, that causes filter clogging, particle wear, breakage, or loss during the adsorption process **[57].**
- Reduced specific surface area and narrow interlayer spacing, which may limit the accessibility of active adsorption sites and negatively affect adsorption performance **[58].**

References

[1]- Yu, Y., Wang, Z., Yao, B., & Zhou, Y. (2024). Occurrence, bioaccumulation, fate, and risk assessment of emerging pollutants in aquatic environments: A review. *Science of The Total Environment*, *923*, 171388.

[2]- Hejna, M., Kapuścińska, D., & Aksmann, A. (2022). Pharmaceuticals in the Aquatic Environment: A Review on Eco-Toxicology and the Remediation Potential of Algae. *International Journal of Environmental Research and Public Health*, *19*(13), 7717.

[3]- Aib, H., Parvez, Md. S., & Czédli, H. M. (2025). Pharmaceuticals and Microplastics in Aquatic Environments: A Comprehensive Review of Pathways and Distribution, Toxicological and Ecological Effects. *International Journal of Environmental Research and Public Health*, *22*(5), 799.

[4]- Boahen, E., Owusu, L., & Adjei-Anim, S. O. (2025). A comprehensive review of emerging environmental contaminants of global concern. *Discover Environment*, *3*(1), 144.

[5]- Mqambalala, A., Maleke, M., Osman, J. R., & Hernandez, J. C. (n.d.). *Biodegradation of Emerging Contaminants Controlled by Biological and Chemical Factors*.

[6]- Amin, M. F., & Rahman, M. S. (2026). Pharmaceutical compounds and their toxicity to marine organisms: Emerging contaminants and innovative strategies to reduce pharmaceutical pollution – A review and meta-analysis. *Comparative Biochemistry and Physiology Part C: Toxicology & Pharmacology*, *305*, 110519.

[7]- Pinto, I., Simões, M., & Gomes, I. B. (2022). An Overview of the Impact of Pharmaceuticals on Aquatic Microbial Communities. *Antibiotics*, *11*(12), 1700.

[8]- Kayode-Afolayan, S. D., Ahuekwe, E. F., & Nwinyi, O. C. (2022). Impacts of pharmaceutical effluents on aquatic ecosystems. *Scientific African*, *17*, e01288.

[9]- Coronado-Apodaca, K. G., Rodríguez-De Luna, S. E., Araújo, R. G., Oyervides-Muñoz, M. A., González-Meza, G. M., Parra-Arroyo, L., Sosa-Hernandez, J. E., Iqbal, H. M. N., & Parra-Saldivar, R. (2023). Occurrence, transport, and detection techniques of emerging pollutants in groundwater. *MethodsX*, *10*, 102160.

[10]- Khan, S., Khan, J. A., & Wei, Z. (2025). Editorial: Emerging trends in advanced oxidation processes for water treatment. *Frontiers in Environmental Chemistry*, *6*, 1693281.

[11]- Nayak, A., Chaudhary, P., Bhushan, B., Ghai, K., Singh, S., & Sillanpää, M. (2024). Removal of emergent pollutants: A review on recent updates and future perspectives on polysaccharide-based composites vis-à-vis traditional adsorbents. *International Journal of Biological Macromolecules*, *258*, 129092.

[12]- Boahen, E., Owusu, L., & Adjei-Anim, S. O. (2025). A comprehensive review of emerging environmental contaminants of global concern. *Discover Environment*, *3*(1), 144.

[13]- Mohamadpour, F., & Amani, A. M. (2024). Photocatalytic systems : Reactions, mechanism, and applications. *RSC Advances*, *14*(29), 20609-20645.

[14]- Ardila-Leal, L. D., Poutou-Piñales, R. A., Pedroza-Rodríguez, A. M., & Quevedo-Hidalgo, B. E. (2021). A Brief History of Colour, the Environmental Impact of Synthetic Dyes and Removal by Using Laccases. *Molecules*, *26*(13), 3813.

[15]- Alzain, H., Kalimugogo, V., & Hussein, K. (2023). A Review of Environmental Impact of Azo Dyes. *International Journal of Research and Review*, *10*(6), 64–689.

[16]- Jassim, A. H., Mohammad, R. K., Ahmed, L. M., & Aboud, L. H. (2022). *Study the optical properties of Congo red dye*. 030002.

[17]- Berradi, M., Hsissou, R., Khudhair, M., Assouag, M., Cherkaoui, O., El Bachiri, A., & El Harfi, A. (2019). Textile finishing dyes and their impact on aquatic environs. *Heliyon*, *5*(11), e02711.

[18]- Panieri, E., Baralic, K., Djukic-Cosic, D., Buha Djordjevic, A., & Saso, L. (2022). PFAS Molecules: A Major Concern for the Human Health and the Environment. *Toxics*, *10*(2), 44.

[19]- Kurwadkar, S., Dane, J., Kanel, S. R., Nadagouda, M. N., Cawdrey, R. W., Ambade, B., Struckhoff, G. C., & Wilkin, R. (2022). Per- and polyfluoroalkyl substances in water and wastewater: A critical review of their global occurrence and distribution. *Science of The Total Environment*, *809*, 151003.

[20]- Alsadik, A., Akintunde, O. O., Habibi, H. R., & Achari, G. (2025). PFAS in water environments: Recent progress and challenges in monitoring, toxicity, treatment technologies, and post-treatment toxicity. *Environmental Systems Research*, *14*(1), 18.

[21]- Liu, Z., Wang, G., Zheng, X., Sepúlveda, M. S., Wang, B., & Zhang, H. (2026). Detection methods, distribution and ecological risks of per- and polyfluoroalkyl substances (PFAS) in aquatic environments: Research advances and future perspectives. *TrAC Trends in Analytical Chemistry*, *200*, 118826.

[22]- Madhav, S., Gupta, H., Srivastav, A. L., & Ahmed, S. (Eds). (2026). *Municipal Sewage and Sludge: Treatment and Disposal Strategies: Management of Sewage and Sludge*. Springer Nature Switzerland.

[23]- Trifirò, F., et al. (2024). Water Purification: Physical, Mechanical, Chemical and Biological Treatments. *Mathews Journal of Pharmaceutical Sciences*, *8*(3), 42.

[24]- Al-Ajmi, F., Al-Marri, M., Almomani, F., & AlNouss, A. (2024). A Comprehensive Review of Advanced Treatment Technologies for the Enhanced Reuse of Produced Water. *Water*, *16*(22), 3306.

[25]- Shamshad, J., & Ur Rehman, R. (2025). Innovative approaches to sustainable wastewater treatment: A comprehensive exploration of conventional and emerging technologies. *Environmental Science: Advances*, *4*(2), 189–222.

[26]- Oakley, S. (2019). Preliminary Treatment and Primary Sedimentation. In Michigan State University, J. B. Rose, B. Jiménez Cisneros, & UNESCO - International Hydrological Programme, *Water and Sanitation for the 21st Century: Health and Microbiological Aspects of Excreta and Wastewater Management (Global Water Pathogen Project)*. Michigan State University.

[27]- Theophilus Ogunwumi, O., Festus Adeniyi, A., Chinazor Angus, M., & Sunday Oche, O. (2024). Biological Wastewater Treatment. In B. Kılıç Taşeli, E. Jacob-Lopes, L. Queiroz Zepka, & M. Costa Deprá (Eds), *Wastewater Treatment and Sludge Management Systems—The Gutter-to-Good Approaches*.

[28]- Ali, S. K., Abdou, M. M., Emara, M. M., Farag, R. S., & Mubarak, M. F. (2025). Eco-friendly solutions: A comprehensive review of natural coagulants for sustainable water treatment. *Environmental Geochemistry and Health*, *47*(12), 535.

[29]- Ihsanullah, I., Mahmoud, A. K., & Jamal, A. (2021). Recent advances on nano-adsorbents and nanomembranes for the remediation of water. *Journal of Cleaner Production*, *322*, 129110.

[30]- Jeevanandam, J., Barhoum, A., Chan, Y. S., Dufresne, A., & Danquah, M. K. (2018). Review on nanoparticles and nanostructured materials: History, sources, toxicity and regulations. *Beilstein Journal of Nanotechnology*, *9*, 1050–1074.

[31]- Hassaan, M. A., El-Nemr, M. A., Elkatory, M. R., Ragab, S., Niculescu, V.-C., & El Nemr, A. (2023). Principles of photocatalysts and their different applications: A review. *Topics in Current Chemistry, 381*(6), 31.

[32]- Mohamadpour, F., & Amani, A. M. (2024). Photocatalytic systems: Reactions, mechanism, and applications. *RSC Advances*, *14*(29), 20609–20645.

[33]- Kraus, K.; Mikziński, P.; Widelski, J.; Paluch, E. Nanomaterials for Photocatalytic Inactivation and Eradication of *Candida* spp. Biofilms in Healthcare Environment: A Novel Approach in Modern Clinical Practice. *Molecules* **2025**, *30* (23), 4500.

[34]- Hadnadjev-Kostic, M., Vulic, T., Karanovic, D., Tomic, A., & Cvetkovic, D. (2025). Layered Double Hydroxide-Based Materials for Wastewater Treatment: Recent Progress in Multifunctional Environmental Applications. *Processes*, *13*(12), 3757.

[35]- Ye, H., Liu, S., Yu, D., Zhou, X., Qin, L., Lai, C., ... & Xiang, L. (2022). Regeneration mechanism, modification strategy, and environment application of layered double hydroxides: Insights based on memory effect. *Coordination Chemistry Reviews*, *450*, 214253.

[36]- Bouziane, Z., Amor, F., Fatine, S., Nunzi, J. M., & Laghzizil, A. (2026). Layered double hydroxide materials for environmental applications: insights on key properties from synthesis and structure. *RSC advances*, *16*(24), 22114-22129.

[37]- Satyam, S., & Patra, S. (2024). Innovations and challenges in adsorption-based wastewater remediation: A comprehensive review. *Heliyon*, *10*(9), e29573.

[38]- Hadnadjev-Kostic, M., Vulic, T., Karanovic, D., Tomic, A., & Cvetkovic, D. (2025). Layered Double Hydroxide-Based Materials for Wastewater Treatment: Recent Progress in Multifunctional Environmental Applications. *Processes*, *13*(12), 3757.

[39] - Song, G. (2025). *Advancements in layered double hydroxide-based materials for food safety detection*.

[40]- Sescu, A. M., Harja, M., Favier, L., Berthou, L. O., Gomez De Castro, C., Pui, A., & Lutic, D. (2020). Zn/La Mixed Oxides Prepared by Coprecipitation: Synthesis, Characterization and Photocatalytic Studies. *Materials*, *13*(21), 4916.

[41]- Zhang, T., Li, Y., & Zheng, W. (2025). Morphological control synthesis of layered double hydroxides for energy applications. *Discover Materials*, *5*(1), 191.

[42]- Chang, C., Rad, S., Gan, L., Li, Z., Dai, J., & Shahab, A. (2023). Review of the sol–gel method in preparing nano TiO_2 for advanced oxidation process. *Nanotechnology Reviews*, *12*(1), 20230150.

[43]- Kim, A., Varga, I., Adhikari, A., & Patel, R. (2021). Recent Advances in Layered Double Hydroxide-Based Electrochemical and Optical Sensors. *Nanomaterials*, *11*(11), 2809.

[44]- Wu, L., Yu, L., Xiao, X., Zhang, F., Song, S., Chen, S., & Ren, Z. (2020). Recent Advances in Self-Supported Layered Double Hydroxides for Oxygen Evolution Reaction. *Research*, *2020*, 2020/3976278.

[45]- Bui, V. K. H., Van Tran, V., Le Tran, H., Do, H. H., Nguyen, M. K., & Hur, J. (2025). Layered double hydroxides and layered double oxides: Multifunctional catalysts for the detection, degradation, and transformation of phenolic compounds in environmental applications. *Environmental Research*, 122711.

[46]- Negm, N. A., Betiha, M. H., Elwakeel, N. M., & Mohamed, E. A. (2023). *Current Advances on Layered Double Hydroxides: Synthetic Routes, Structure Modification, Characterization, Topical Applications, and Future Prospects*. *2*.

[47]- Altalhi, A. A., Mohamed, E. A., & Negm, N. A. (2024). Recent advances in layered double hydroxide (LDH)-based materials: fabrication, modification strategies, characterization, promising environmental catalytic applications, and prospective aspects. *Energy Advances*, *3*(9), 2136-2151.

[48]- Mohamed, F., Salem, O. M., Abdelkarem, K., Shaban, M., & Ahmed, A. M. (2025). Experimental and theoretical insights into LDH based on iron for photoelectrochemical water splitting. *Scientific Reports*, *15*(1), 35801.

[49]- Mureseanu, M., Cioatera, N., & Carja, G. (2023). Fe-Ce/layered double hydroxide Heterostructures and their derived oxides: Electrochemical characterization and light-driven catalysis for the degradation of phenol from water. *Nanomaterials*, *13*(6), 981.

[50]- Krishnan, A., Ajith, A., Krishnan, A. V., Saji, R. E., Syamli, S., & Shibli, S. M. A. (2023). Ni-Based electro/photo-catalysts in HER–a review. *Surfaces and Interfaces*, *36*, 102619.

[51]- Zhu, C., & Wang, X. (2025). Nanomaterial ZnO synthesis and its photocatalytic applications: A review. *Nanomaterials*, *15*(9), 682.

[52]- Gama, B. M. V. D., Selvasembian, R., Giannakoudakis, D. A., Triantafyllidis, K. S., McKay, G., & Meili, L. (2022). Layered double hydroxides as rising-star adsorbents for water purification: A brief discussion. *Molecules*, *27*(15), 4900.

[53]- Crini, G., Lichtfouse, E., Wilson, L. D., & Morin-Crini, N. (2019). Conventional and non conventional adsorbents for wastewater treatment. *Environmental Chemistry Letters*, *17*(1), 195–213. https://doi.org/10.1007/s10311-018-0786-8

[54]- Yang, Z., Wang, F., Zhang, C., Zeng, G., Tan, X., Yu, Z., ... & Cui, F. (2016). Utilization of LDH-based materials as potential adsorbents and photocatalysts for the decontamination of dyes wastewater: a review. *RSC advances*, *6*(83), 79415-79436.

[55]- Vievard, J., Alem, A., Pantet, A., Ahfir, N. D., Arellano-Sánchez, M. G., Devouge-Boyer, C., & Mignot, M. (2023). Bio-based adsorption as ecofriendly method for wastewater decontamination: a review. *Toxics*, *11*(5), 404.

[56]- Kobylinska, N., Puzyrnaya, L., & Pshinko, G. (2022). Magnetic nanocomposites based on Zn, Al-LDH intercalated with citric and EDTA groups for the removal of U (VI) from

environmental and wastewater: synergistic effect and adsorption mechanism study. *RSC advances*, *12*(50), 32156-32172.

[57]- Pan, Y., Li, L., Liu, D., Wang, F., Xia, M., & Wang, F. (2025). Macroscale structures of layered double hydroxides: A review of formation strategies and applications in water treatment. *Journal of Environmental Chemical Engineering*, *13*(1), 115284.

[58]- Xu, T., Fei, C., Zhou, H., Fan, Y., Tang, K., Chen, C., ... & Mao, R. (2025). The formation and adsorption mechanism studies of three-dimensional (3D flower-like) layered double hydroxide. *Applied Surface Science*, *691*, 162671.

Chapter II :

Materials & Techniques

Chapter II : Materials & Techniques

This chapter aimed to synthesize and characterize the LDO-based catalysts for the degradation of an organic dye in aqueous media; this catalyst is obtained by the calcination of LDH at high temperature, which is elaborated via the co-precipitation method.

II.1 Chemicals

Zinc nitrate hexahydrate (**$Zn(NO_3)_2 \cdot 6H_2O$**), nickel (II) nitrate tetrahydrate (**$Ni(NO_3)_2 \cdot 4H_2O$**), and sodium carbonate (Na_2CO_3) were procured from Sigma-Aldrich, Co., Germany. Iron (III) nitrate nonahydrate (**$Fe(NO_3)_3 \cdot 9H_2O$**) and sulfuric acid (H_2SO_4, 95–97%) were obtained from Honeywell Fluka, Co., Germany. Sodium hydroxide (NaOH) was supplied by SpeciLab. These chemicals were used as precursors, pH-regulating agents, and precipitating agents during the synthesis process. Congo Red (CR, **$C_{32}H_{22}N_6Na_2O_6S_2$**), an anionic diazo dye commonly used in the textile industry, was employed as the adsorbate in the experiments.

All chemicals were of analytical grade and were used as received without further purification.

II.2 Target pollutant: Congo red dye (CR)

Congo Red (CR) is a water-soluble anionic diazo dye extensively employed in textile, plastic, cosmetic, and pharmaceutical applications. The dye contains azo (–N=N–) linkages that impart high chemical stability and resistance to biodegradability.

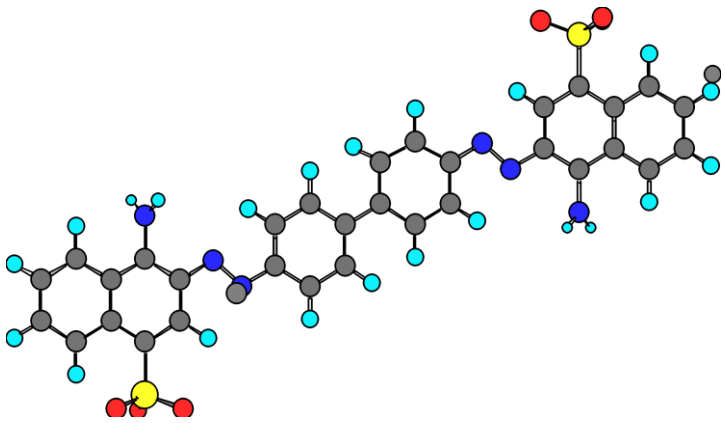

Fig.II.1. *Congo red's 3D chemical structure* [1].

Due to its persistence in the environment and its potential harmful effects, including carcinogenicity and toxicity to the skin, respiratory, ocular, and reproductive systems, the effective removal of CR from wastewater has become an important objective in environmental remediation and water treatment processes **[2, 3].**

The main characteristics and the three-dimensional chemical structure of CR are presented in **Table II.1** and **Fig.II.1** respectively.

Table II.1: *Main characteristics of CR as an adsorbate [4].*

Property	Description
Common name	Congo red
IUPAC name	Sodium salt of 3,3'-([1,1'-biphenyl]-4,4'-diyl) bis (4-aminonaphtalene-1-sulfonic acid)
Molecular formula	$C_{32}H_{22}N_6Na_2O_6S_2$
Molecular weight	696,67g/mol
Dye class	Anionic azo dye (-N=N-)
Λ_{max}	497nm

II.3 Required equipment

The successful implementation of the experimental protocol required the use of specialized equipment available in our Chemistry Laboratory of the University of Chadli Bendjedid El-Tarf.

The instruments listed in Table II.2 were carefully selected based on the specific requirements of each stage of the synthesis and treatment process. Each piece of equipment plays a distinct and essential role, ranging from the precise preparation and weighing of reagents, to the control of solution pH, thermal treatment, and the separation and homogenization of the synthesized materials. The model and function of each instrument are specified to ensure reproducibility and to guide the procurement process.

Table II.2: *Required laboratory equipment, models, and their functions.*

Equipment	Model / Product	Image	Function
Magnetic Hotplate Stirrer	Stuart Hotplate Stirrer		Heating and stirring of solutions.
Analytical Balance	OHAUS Pioneer PX Series	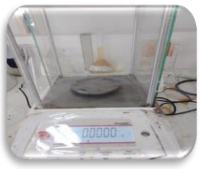	Precise weighing of reagents and samples.
pH Meter	Bench-top pH Meter		Measurement and adjustment of pH.
Centrifuge	Sigma 3-16L Benchtop Centrifuge		Separation of precipitates from suspensions by centrifugal force.
Drying Oven	Memmert Laboratory Oven		Drying of synthesized materials.
Muffle Furnace	Nabertherm Muffle Furnace		Calcination and thermal treatment of samples.
Mortar and pestle	Agate Mortar and Pestle	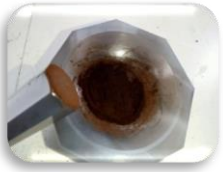	Grinding and homogenization of powders.

II.4 Co-precipitation synthesis method

The co-precipitation method is considered as the most commonly used technique to produce LDHs. In this process, metal cations (M^{2+} and M^{3+}) are simultaneously precipitated from an aqueous solution by raising the pH to alkaline conditions using a base,

while the anions meant to fill the interlayer space are incorporated at the same time, resulting in the direct formation of the LDH structure **[5].**

II.5 Synthesis procedure

The synthesis of the catalyst was carried out through a series of sequential steps. The procedure involves dissolving the precursor reagents, followed by precipitation, aging, washing, drying, calcination, grinding, and finally catalyst activation. Each step was carefully controlled to ensure the production of a material with optimal physicochemical properties.

a. Dissolving : The metal salts $Zn(NO_3)_2$, $Ni(NO_3)_2$, and $Fe(NO_3)_3$ were dissolved/dispersed individually in a partial volume of water, then mixed and adjusted to the final volume **150 mL** at a final concentration of **0.1 M**, under magnetic stirring at **400 rpm** and room temperature.

Fig.II.2. *Preparation of precursor solution.*

b. Precipitation: A mix of the basic solution was prepared from a **75 mL** of NaOH **(2 M)** and **75 mL** of Na_2CO_3 **(0.5 M)** at a ratio **1:1**, which was added dropwise while the pH was continuously monitored.

If necessary, adjustment was carried out using the diluted NaOH solution to reach **pH** = **9**, with the temperature maintained **± 2°C**.

c. Aging: the mixture was left stirring **(400 rpm)** for **18h** at **60°C**.

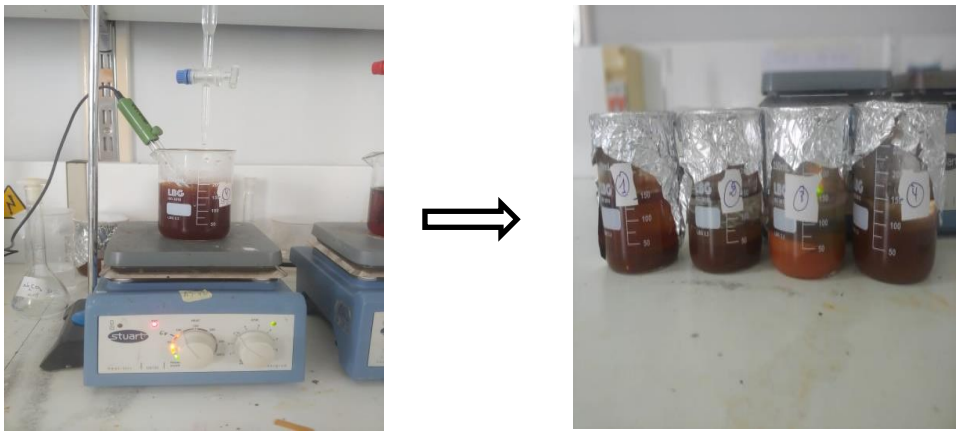

Fig.II.3. *Aging of the precipitate.*

d. Washing : the precipitate was washed by centrifugation at 4000rpm for 10min, followed by the elimination of supernatant. Then a **10** to **20mL** of distilled water was added and stirred for 2 to 3min before each cycle, this step was repeated at least 5 times until the final pH reached 7.

e. Drying : after washing the solution, the recovered solid was dried in a ventilated oven at **70°C** for 12 to 16 h before it was stored in a glass box or crucible for drying.

f. Calcination : heat treatment process that thermally decomposes the LDH precursor into a mixed metal oxide (LDO) by eliminating water and carbonate groups through successive temperature stages.

Table.II.3: *Calcination conditions used for LDH synthesis.*

Temperature	Duration	Purpose
120°C	**1h**	Evaporation of residual moisture.
300°C	**2h**	Decomposition of hydroxyl groups and carbonates.
550°C	**3h**	Complete conversion into LDO phase.
Room temperature	**Natural**	Slow cooling to avoid thermal shock and stabilize the oxide phase.

Transformation: LDH→Fe_2O_3+NiO+CuO+H_2O+CO_2

g. Grinding: was carried out using an agate mortar for **10-15 min** until a fine homogeneous powder was obtained.

h. Catalyst activation: under **110 °C** for an hour the catalyst was activated, to eliminate the residual moisture and was then stored in an airtight container away from humidity.

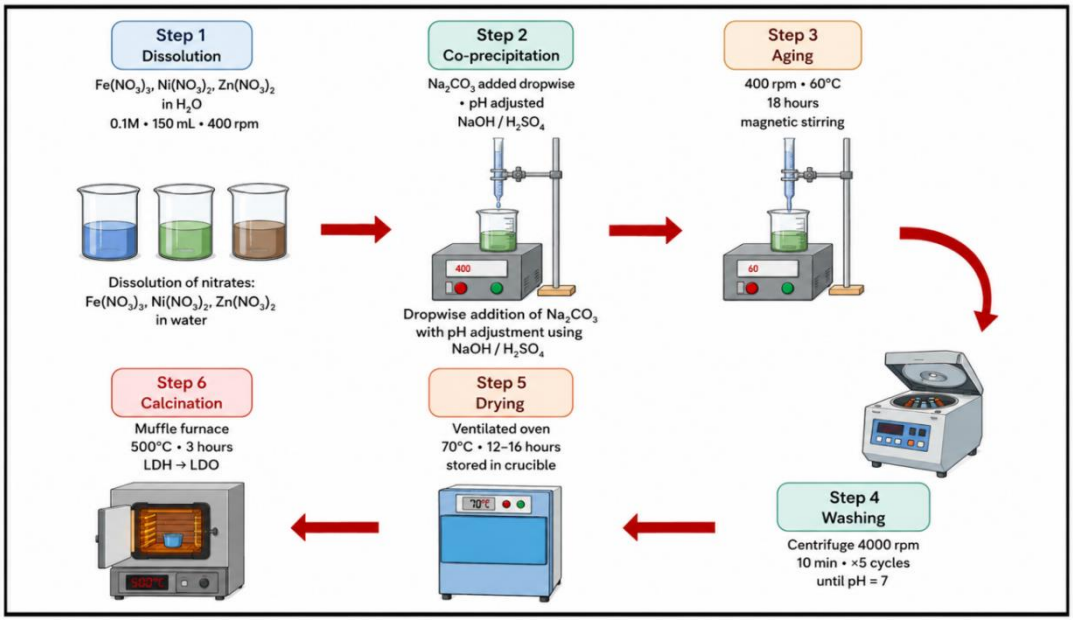

Fig.II.4. *Experimental workflow of Fe-Ni-Zn LDH/LDO synthesis.*

II.6 Characterization techniques

The characterization techniques were performed to confirm the successful synthesis of the LDH and to evaluate its structural, morphological, thermal, and optical properties.

II.6.1 UV-visible spectroscopy

UV-Vis spectroscopy is a qualitative and analytical method based on the measurement of discrete UV or visible light wavelengths that are either absorbed or transmitted by a sample when compared to a blank or reference sample.

The technique operates within a wavelength range from 200 nm to 800 nm, covering the UV region from 200 nm to 400 nm and the visible region from 400 nm to 800 nm. When light interacts with the sample, adsorption peaks appear in the spectrum at positions corresponding to specific electronic transitions occurring within the sample molecules, providing valuable information for the identification and quantification of the compound present **[6].**

It's used to investigate the optical properties of the synthesized LDH and LDO samples practically to identify the characteristic absorption bands associated with the metal ions (Ni^{2+}, Zn^{2+}, Fe^{3+}) and to estimate the optical band gap energy.

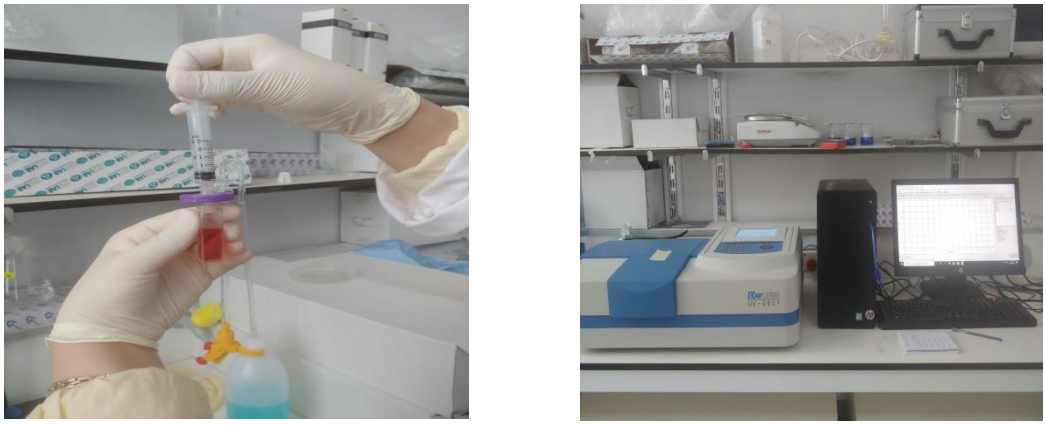

Fig.II.5. *Rayleigh UV-2601 double beam spectrophotometer used for UV-Vis analysis.*

II.6.2 X-Ray diffraction (XRD)

X-Ray Diffraction (XRD) is a non-destructive analytical technique that delivers comprehensive information on a materials crystallographic structure, chemical composition, and physical properties. XRD peaks arise from the constructive interference of a monochromatic X-ray beam as it is scattered at specific angles by the various lattice planes within a sample (**Fig.II.6)**.

The intensity of each peak reflects the spatial arrangement of atoms within the crystal lattice. As a result, the X-ray diffraction pattern serves as a unique fingerprint representing the periodic atomic arrangement of a given material **[7].**

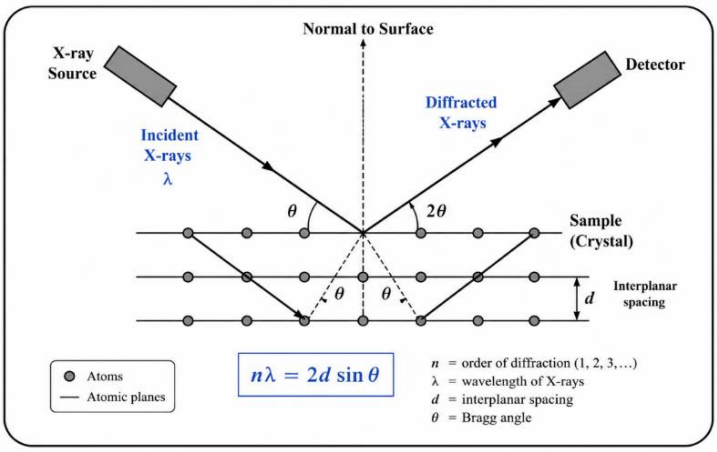

Fig.II.6. *Schematic Diagram of X-Ray Diffraction (XRD) Based on Bragg's Law* [8].

When a beam of X-ray photons interacts with a crystalline sample, part of the radiation is diffracted with a wavelength λ at specific angles **θ**. These angles are directly related to the interplanar spacing **d** through Bragg's law:

$$2d_{hkl}\sin\theta = n\lambda \qquad (\mathbf{II.1})$$

Where λ is the wavelength of the incident X-ray beam, θ is the Bragg angle, n is an integer representing the order of diffraction, and d_{hkl} is the spacing between crystallographic planes belonging to the same family (hkl). **Fig.II.6 and 7** illustrates the diffraction principle for a family of crystallographic planes. The diffraction peaks are identified by comparison with the standard JCPDS-ICDD database **(**Joint Committee on Powder Diffraction Standards_ International Centre for Diffraction Data), which allows the indexing of crystallographic planes and the determination of the material structure.

XRD measurements of the investigated samples were performed using a Bruker D8 diffractometer **Fig.II.6** in Bragg–Brentano (**θ–2θ**) geometry, employing **Cu K_α** radiation with a wavelength of **λ = 0.154056 nm**. The samples were carefully prepared to ensure a homogeneous surface area of at least **1 cm²**.

To achieve good data quality, the scans were recorded with an angular step size of **2θ = 0.02°**, and a counting time of **9 s** per step. This technique enables the determination of crystallographic parameters as well as the identification of microstructural imperfections such as crystallite size reduction and lattice distortions.

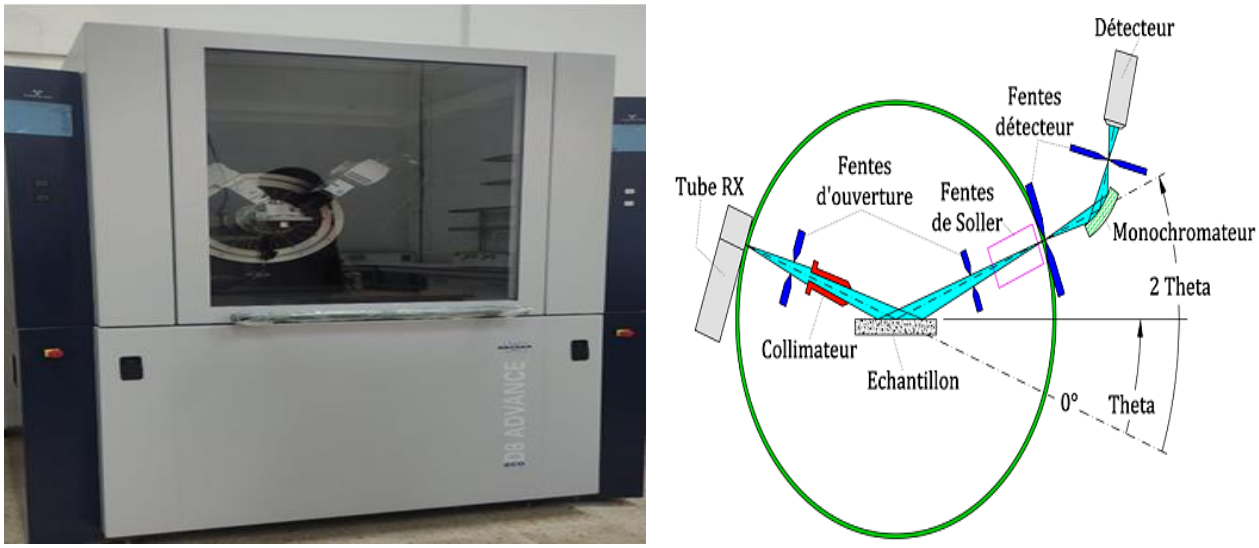

Fig.II.7. *BRUKER D8 ADVANCE X-ray Diffractometer used machine.*

II.6.3 FTIR spectroscopy

Fourier Transform Infrared Spectroscopy (**FTIR**, **Fig.II.8),** relies on the fact that different bonds in a molecule will vibrate at very specific frequencies when exposed to infrared (IR) light. Such vibrations are directly related to the molecular structure, rendering FTIR a very important tool for the identification and characterization of chemical compounds through the measurement of its interaction with IR radiation.

The IR radiation spectrum covers three main regions: the near-IR from 14000 to 4000cm^{-1}, the mid-IR 4000 to 400cm^{-1} , and the far-IR from 400 to 10cm^{-1} **[9].**

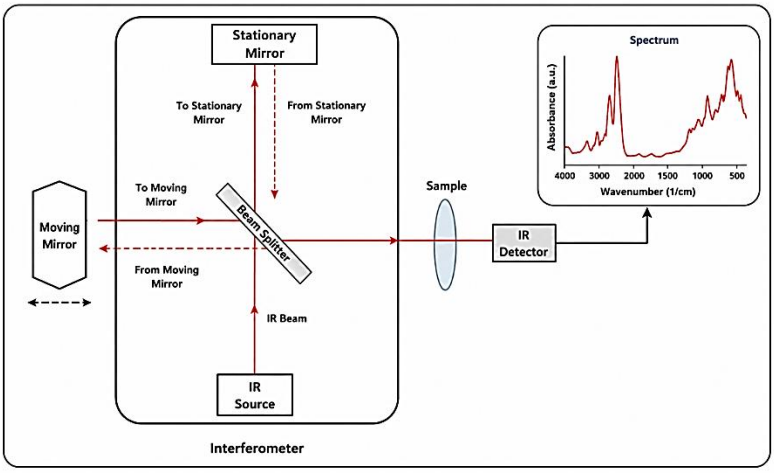

Fig.II.8. *Principle of Fourier Transform Infrared (FTIR) spectroscopy [10].*

II.6.4 Simultaneous thermal analysis (STA)

According to the International Confederation for Thermal Analysis **(ICTA)** recommendation on nomenclature in thermal analysis, the term "simultaneous techniques" is defined as the application of two or more techniques to the same sample at the same time **[11]**.

The differential scanning calorimetry (**DSC**, **Fig.II.9**), coupled with thermogravimetric analysis (**TGA**), allows the simultaneous investigation of thermal effects and mass variations associated with physicochemical transformations of materials as a function of temperature. This combined technique is particularly useful for analyzing dehydration, decomposition, crystallization phenomena, as well as phase transitions. The measurement principle is based on the comparison of heat flow between a sample and an inert reference, while simultaneously recording the mass changes of the sample during heating **[12].**

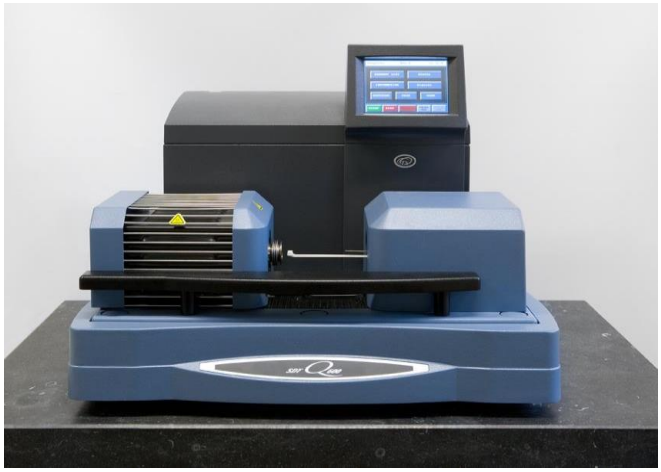

***Fig.II.9. Q600** simultaneous **TGA/DSC** instrument.*

The **DSC** signal corresponds to enthalpic events (endothermic or exothermic processes), whereas the **TGA** signal monitors mass losses or gains associated with chemical transformations. For the materials investigated in this work, this technique is particularly effective in identifying successive stages of dihydroxylation, decarbonation, and phase transformation, especially the conversion of layered double hydroxides (LDH) into mixed oxides (LDO). The obtained thermograms therefore allow correlation of thermal events with structural changes observed by X-ray diffraction (XRD) **[13].**

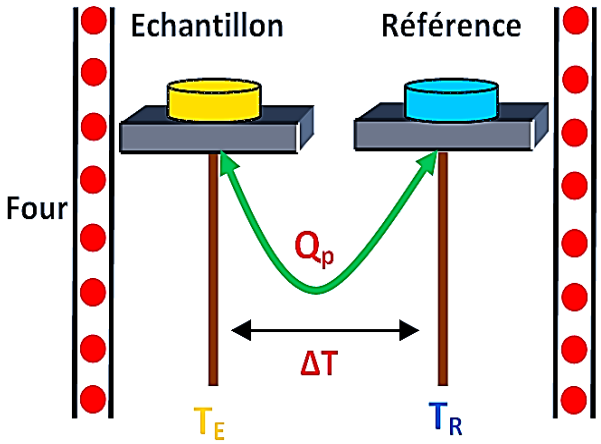

***Fig.II.10.** Schematic diagram of the TGA/DSC principle.*

Thermal analyses were performed using a **Q600** simultaneous thermogravimetric analyzer coupled with differential scanning calorimetry (**TGA/DSC**), under an argon atmosphere in order to avoid any undesired oxidation during heating. The heating rate was set at **10 °C/min**, with a temperature precision of approximately **± 0.01 °C**. The analyzed samples had a typical mass of **16 ± 2 mg** and were heated over a temperature range from 25 to 1000 °C. Characteristic temperatures (such as mass loss, decomposition, or phase

transformation temperatures) were determined from the **TGA** and **DSC** curves with an estimated uncertainty greater than **0.2 °C [13].**

II.6.5 3D Optical Profilometry

An optical 3D surface profilometer, also referred to as optical surface profiler, is a non-contact instrument designed to precisely capture the surface morphology of an object and extract three-dimensional depth information through optical means. Its primary function is to map surface elevation as a function of lateral position across a defined area, a capability that sets it apart from conventional microscopes, where image contrast is governed by various optical properties of the sample that often has no direct relation to the actual topological features of the surface **[14].** Typically, these systems rely on an optical beam pattern generator module to produce various structured light patterns; from which depth data is derived by analyzing the distortions introduced when the patterns are projected onto the target surface **[15].**

II.7 Conclusion

This chapter described the materials and experimental procedures used in our work, including the synthesis LDO, and its characterization by various analytical techniques, the adopted methodology ensures the reliability and reproducibility of the obtained results, which are analyzed and discussed in the next chapter.

References

[1]- Ali, N., Uddin, S., Khan, A., Khan, S., Khan, S., Ali, N., ... & Bilal, M. (2020). Regenerable chitosan-bismuth cobalt selenide hybrid microspheres for mitigation of organic pollutants in an aqueous environment. International journal of biological macromolecules, 161, 1305-1317.

[2]- Semwal, N., Mahar, D., Chatti, M., Dandapat, A., & Arya, M. C. (2023). Adsorptive removal of Congo Red dye from its aqueous solution by Ag–Cu–CeO_2 nanocomposites: Adsorption kinetics, isotherms, and thermodynamics. Heliyon, 9(11).

[3]- Ak, B., Gul, E. M., Senberber-Dumanli, F. T., Kipcak, A. S., & Derun, E. M. (2026). Congo Red Photodegradation using Magnesium Borate under UV Irradiation and Modelling by the Box Behnken Method. Water, Air, & Soil Pollution, 237(8), 485.

[4]- Odhaib, W. Y., Jaeel, A. J., & Wadees, C. (2023). Color and COD removal from textile effluent using alum and $FeCl_3$ coagulation. Wasit Journal of Engineering Sciences, 11(1), 126-133.

[5]- Negm, N. A., Betiha, M. H., Elwakeel, N. M., & Mohamed, E. A. (2023). Current Advances on Layered Double Hydroxides: Synthetic Routes, Structure Modification, Characterization, Topical Applications, and Future Prospects. 2.

[6]- Dubey, R., Kumar, A., & Gupta, B. K. (2024). A REVIEW OF UV-VISIBLE SPECTROSCOPY: TECHNIQUES AND APPLICATIONS. 9(10).

[7]- Ali, A., Chiang, Y. W., & Santos, R. M. (2022). X-ray diffraction techniques for mineral characterization: A review for engineers of the fundamentals, applications, and research directions. Minerals, 12(2), 205.

[8]- Xu, Y., Zhou, Y., Li, Y., & Zheng, Y. (2024). Bridging Materials and Analytics: A comprehensive review of characterization approaches in metal-based solid-state hydrogen storage. Molecules, 29(21), 5014.

[9]- Al-Amin, K., Kawsar, Md., Mamun, Md. T. R. B., & Sahadat Hossain, Md. (2025). Fourier transform infrared spectroscopic technique for analysis of inorganic materials: A review. Nanoscale Advances, 7(21), 6677–6702.

[10]- Faghihzadeh, F., Anaya, N. M., Schifman, L. A., & Oyanedel-Craver, V. (2016). Fourier transform infrared spectroscopy to assess molecular-level changes in microorganisms exposed to nanoparticles. Nanotechnology for Environmental Engineering, 1(1), 1.

[11]- Wesolowski, M., & Leyk, E. (2023). Coupled and Simultaneous Thermal Analysis Techniques in the Study of Pharmaceuticals. Pharmaceutics, 15(6), 1596.

[12]- Hitachi High-Tech Analytical Science. *Understanding Simultaneous Thermogravimetric Analysis (STA).* AZoM, 2024.

[13]- Leyva-Porras, C., Cruz-Alcantar, P., Espinosa-Solís, V., Martínez-Guerra, E., Piñón-Balderrama, C. I., Compean Martínez, I., & Saavedra-Leos, M. Z. (2019). Application of Differential Scanning Calorimetry (DSC) and Modulated Differential Scanning Calorimetry (MDSC) in Food and Drug Industries. Polymers, 12(1), 5.

[14]- RP Photonics AG. (2026). Optical profilometers. RP Photonics Encyclopedia.

[15]- Joo, K.-I., Kim, M., Park, M.-K., Park, H., Kim, B., Hahn, J., & Kim, H.-R. (2016). A 3D Optical Surface Profilometer Using a Dual-Frequency Liquid Crystal-Based Dynamic Fringe Pattern Generator. Sensors, 16(11), 1794.

Chapter III :

Results & discussion

Chapter III: Results and Discussion

This chapter brings together the experimental results obtained throughout our work. We begin by examining the characteristics of the synthesized NiZnFe-LDO, before turning to its behavior in the adsorption of Congo red dye, with the aim of understanding how and why the process unfolds the way it does.

III.1 UV-visible spectroscopy

The CR stock solution was prepared by dissolution of the dye in distilled water of a concentration of 1000 mg L^{-1}. The prepared stock solution was then diluted into different dye concentrations 2-12 mg·L^{-1} (ppm) as shown in Figure III.1 (b). The quantitative determination of CR demonstrated in **Figure III.1** (a) was performed by Rayleigh UV-2601 double beam spectrophotometer. At a maximum absorption wavelength of $\boldsymbol{\lambda_{max}}$ **= 497 nm**, the calibration curve was constructed by measuring the absorbance the series of the standard aqueous solutions over the previously mentioned concentration. The resulting linear regression equation was :

$$\boldsymbol{A = 0,05353 + 0,05126C} \qquad \textbf{(III. 1)}$$

Where A is the absorbance, and C is the concentration expressed in mg·L^{-1}. The coefficient of determination (**R^2 = 0.99934**) confirms excellent linearity over the investigated concentration range, demonstrating full compliance with the Beer-Lambert law. The high R^2 value, approaching unity, validates the reliability and accuracy of the calibration model and its suitability for the quantitative spectrophotometric determination of CR in aqueous media.

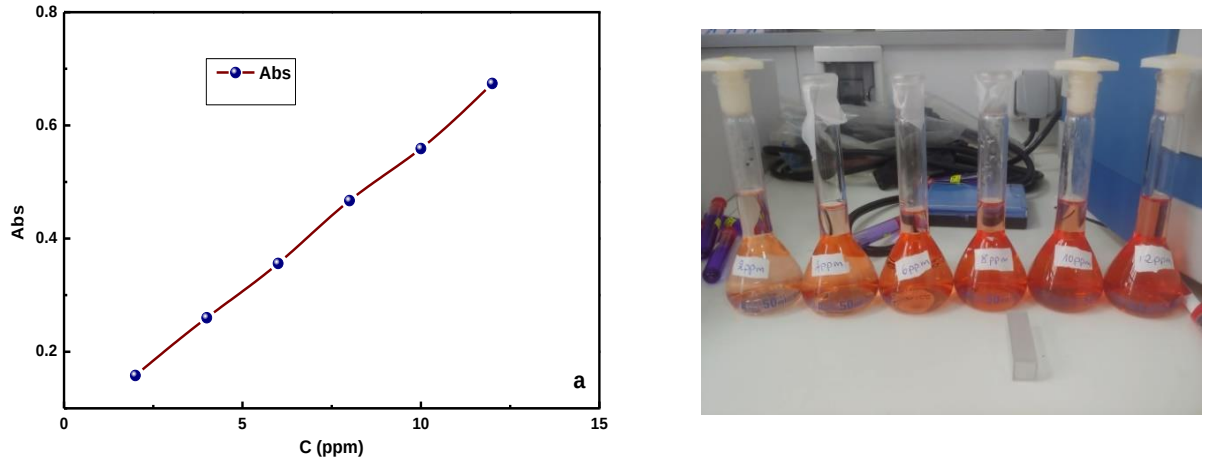

Fig.III.1. *Standard Preparation and Calibration Curve for Quantitative Analysis: (a) Standard calibration plot; (b) Corresponding volumetric flask standards.*

III.2 X-ray Diffraction Analysis (XRD)

X-ray diffraction (XRD) analysis was performed to investigate the crystalline structure, phase purity, and structural transformation of the synthesized $ZnNiFeCO_3$-LDH precursor and the corresponding calcined $ZnNiFeCO_3$-LDO material. The XRD patterns of both samples are presented in **Fig.III.2**.

The XRD pattern of the $ZnNiFeCO_3$-LDH precursor exhibits a series of sharp and well-defined diffraction peaks, indicating a high degree of crystallinity and the successful formation of a hydrotalcite like layered double hydroxide (LDH) structure. The most intense basal reflections are observed at low diffraction angles, particularly at 2θ values around 11° and 23°, corresponding to the (**003**) and (**006**) crystallographic planes, respectively. These characteristic reflections confirm the regular stacking of positively charged brucite like layers, where Zn^{2+} and Ni^{2+} divalent cations are partially substituted by Fe^{3+} trivalent cations. This cationic substitution creates a positive charge imbalance in the hydroxide sheets, which is compensated by the intercalation of carbonate anions (CO_3^{2-}) and water molecules within the interlayer galleries **[1,2]**.

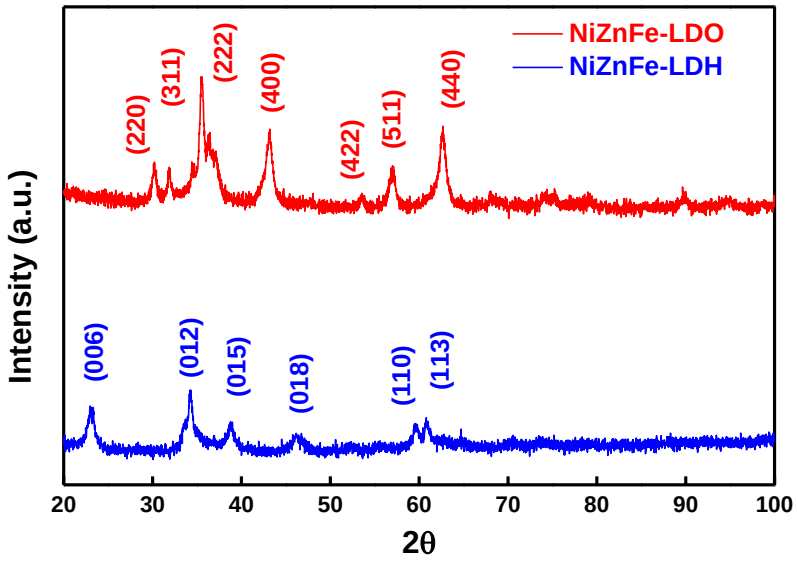

Fig.III.2. *XRD patterns of NiZnFe CO_3-LDH and NiZnFe CO_3-LDO.*

Additional reflections appearing at approximately 2θ ≈ 34°, 39°, 46°, 60°, and 62° are indexed to the (012), (015), (018), (110), and (113) planes, respectively, further confirming the formation of a well-crystallized LDH phase with a typical rhombohedral layered structure. The absence of additional peaks corresponding to individual hydroxides or oxides such as

$Zn(OH)_2$, $Ni(OH)_2$, or Fe_2O_3 suggests that Zn^{2+}, Ni^{2+}, and Fe^{3+} ions are homogeneously incorporated into the LDH lattice rather than forming separate phases **[1,3]**.

The structural parameters of the LDH phase can be determined from the interplanar distances calculated using Bragg's law. The lattice parameter **a**, related to the average distance between neighboring metal cations within the brucite-like sheets, is calculated from the (110) reflection according to the relationship :

$$\mathbf{a = 2d_{110}} \qquad \textbf{(III.2)}$$

whereas the lattice parameter **c**, corresponding to the periodicity along the c-axis and related to the interlayer distance, can be estimated from the basal (003) reflection using:

$$\mathbf{c=3d_{003}} \qquad \textbf{(III.3)}$$

These parameters provide insight into the structural organization and cationic distribution within the LDH framework **[2,4]**.

After calcination at 550 °C for 3 h, significant changes are observed in the XRD pattern of the resulting $ZnNiFeCO_3$-LDO material. The complete disappearance of the characteristic LDH reflections, especially the (003) and (006) peaks, confirms the collapse of the layered structure due to the dehydroxylation of hydroxide layers and the decarbonation of interlayer carbonate species, resulting in the release of H_2O and CO_2 molecules **[1,5]**.

The thermal treatment promotes the rearrangement of Zn^{2+}, Ni^{2+}, and Fe^{3+} cations into a new mixed oxide phase. Consequently, new diffraction peaks emerge at approximately $2\theta \approx 30.2°$, 35.6°, 43.1°, 57.0°, and 62.8°, corresponding to the (220), (311), (400), (511), and (440) crystallographic planes, respectively. These reflections are characteristic of a cubic spinel structure with the *Fd-3m space group*, corresponding to Zn–Ni–Fe mixed oxides such as $ZnFe_2O_4$ and $NiFe_2O_4$. The absence of diffraction peaks associated with separate ZnO, NiO, or α-Fe_2O_3 phases indicates the formation of a homogeneous mixed spinel oxide **[6,7]**.

The crystallite size of the obtained $ZnNiFeCO_3$-LDO material can be estimated from the broadening of the most intense (311) diffraction peak using the **Debye–Scherrer** equation:

$$\boldsymbol{D = \frac{K\lambda}{\beta\cos\theta}} \qquad (\textbf{III. 4})$$

where **D** is the average crystallite size, **K** is the shape factor (0.89), **λ** is the wavelength of Cu Kα radiation (0.15406 nm), **β** is the full width at half maximum (FWHM) of the diffraction peak expressed in radians, and **θ** is the Bragg angle.

The average crystallite size was estimated to be approximately 11.5 nm, indicating the formation of nanocrystalline spinel particles. The nanoscale dimensions are expected to contribute to a higher specific surface area and a larger number of surface defects, which are beneficial for adsorption processes. Furthermore, the cubic lattice parameter of the spinel phase is calculated using the following equation:

$$\boldsymbol{a = d_{hkl}\sqrt{h^2+k^2+l^2}} \qquad (\mathbf{III.5})$$

The lattice parameter of the cubic spinel phase was determined from the main diffraction reflections ((220), (311), (400), (511), and (440)) using Bragg's law to calculate the interplanar spacing (d_{hkl}) and the cubic lattice equation. The average lattice parameter was found to be approximately 8.36 Å, which lies between the reported values of $ZnFe_2O_4$ (≈ **8.44 Å**) and $NiFe_2O_4$ (≈ **8.33 Å**), confirming the successful incorporation of Zn^{2+} and Ni^{2+} ions into the spinel lattice and the formation of a homogeneous Zn–Ni–Fe mixed spinel solid solution **[7,8].**

Overall, the comparison of the XRD patterns before and after calcination clearly demonstrates the successful transformation of the $ZnNiFeCO_3$-LDH precursor into a $ZnNiFeCO_3$-LDO mixed oxide. The collapse of the layered structure and the formation of a nanocrystalline spinel phase are accompanied by the generation of structural defects and mesoporous domains due to the removal of interlayer water, hydroxyl groups, and carbonate anions. These characteristics, combined with the homogeneous distribution of metal cations and small crystallite size, are expected to enhance the adsorption performance of $ZnNiFeCO_3$-LDO toward the removal of pollutants from aqueous solutions **[5,6]**.

III.3 Zero-charge point (pH_{PZC})

The point of zero charge (pH_{PZC}) is an important surface property that determines the surface charge behavior of an adsorbent in aqueous solutions and significantly influences the adsorption of ionic pollutants. The pH_{PZC} corresponds to the pH value at which the net surface charge of the adsorbent is zero. At pH values below the pH_{PZC}, the surface hydroxyl groups become protonated, resulting in a positively charged surface, while at pH values above the pH_{PZC}, deprotonation of these groups occurs, generating a negatively charged surface **[9,10]**.

The pH_{PZC} of ZnNiFe-LDO was determined using the pH drift method. The variation of the final pH (pH_f) as a function of the initial pH (pH_i) and the plot of ΔpH (pH_f - pH_i) versus pH_i are presented in **Fig.III.3(a**) and **Fig.III.3(b)**, respectively.

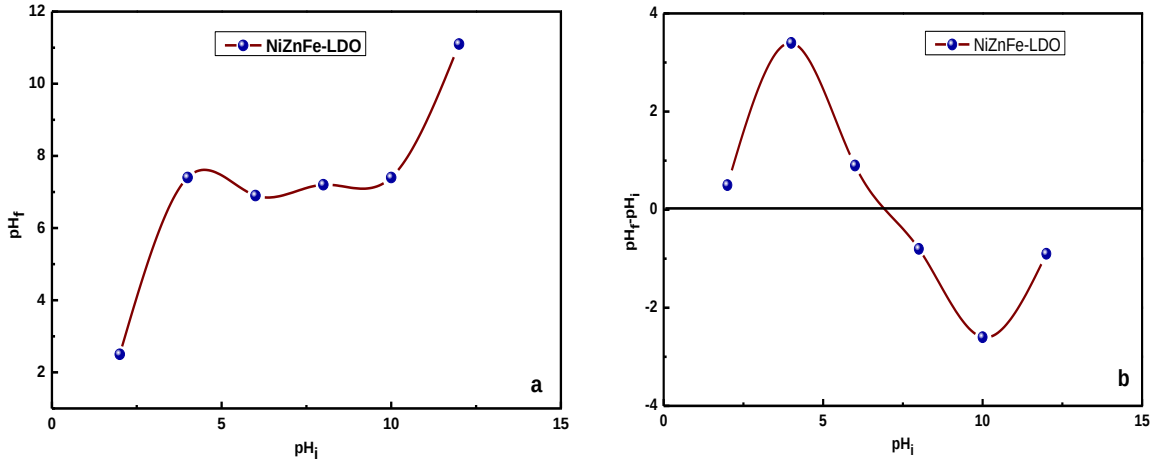

Fig.III.3. *Determination of the pH_{PZC} of ZnNiFe-LDO: (a) final pH (pH_f) as a function of initial pH (pH_i); (b) ΔpH (pH_f − pH_i) as a function of initial pH.*

The pH_{PZC} value was determined from the intersection point where $pH_f = pH_i$ or where ΔpH = 0, and was found to be approximately **6.9**.

The obtained pH_{PZC} value indicates that the surface of ZnNiFe-LDO is positively charged under acidic conditions (pH < 6.9) due to the protonation of surface hydroxyl groups (–OH + H^+ → $–OH_2^+$). Under these conditions, strong electrostatic attractions occur between the positively charged surface of the adsorbent and the negatively charged sulfonate groups ($–SO_3^-$) of Congo Red molecules, leading to enhanced adsorption efficiency **[11,12]**.

In contrast, at pH values higher than 6.9, the surface hydroxyl groups undergo deprotonation (–OH → $–O^-$ + H^+), resulting in a negatively charged surface. Consequently, electrostatic repulsion between the negatively charged ZnNiFe-LDO surface and the anionic CR molecules may reduce the adsorption capacity. Nevertheless, the adsorption process is not exclusively controlled by electrostatic interactions. Other mechanisms, including hydrogen bonding, surface complexation, and possible interactions between the aromatic structure of CR and active surface sites, may also contribute to the adsorption process **[2,13]**.

The pH_{PZC} value close to neutrality (6.9) indicates a balanced surface acidity/basicity, which is advantageous for practical wastewater treatment because many natural waters exhibit a

near-neutral pH. Combined with the nanocrystalline spinel structure, a high density of active surface sites, and the porous structure commonly obtained after the calcination of LDH precursors, ZnNiFe-LDO exhibits favorable physicochemical characteristics for the efficient adsorption and removal of CR from aqueous solutions.

III.4 Three-dimensional optical microscopy analysis

The three-dimensional optical microscopy image of the synthesized $ZnNiFeCO_3$-LDO material recorded at a magnification of ×50 is presented in **Fig.III.4**. The surface topography reveals a relatively homogeneous distribution of irregular elevations and depressions, resulting in a rough and heterogeneous surface morphology. The 3D height profile and color contrast indicate significant variations in surface relief, suggesting the presence of numerous surface asperities and valleys distributed over the analyzed area.

The observed roughness can be associated with the structural modifications induced by the calcination of the $ZnNiFeCO_3$-LDH precursor, including the removal of interlayer water, hydroxyl groups, and carbonate species, leading to the collapse of the layered structure and the formation of mixed metal oxides.

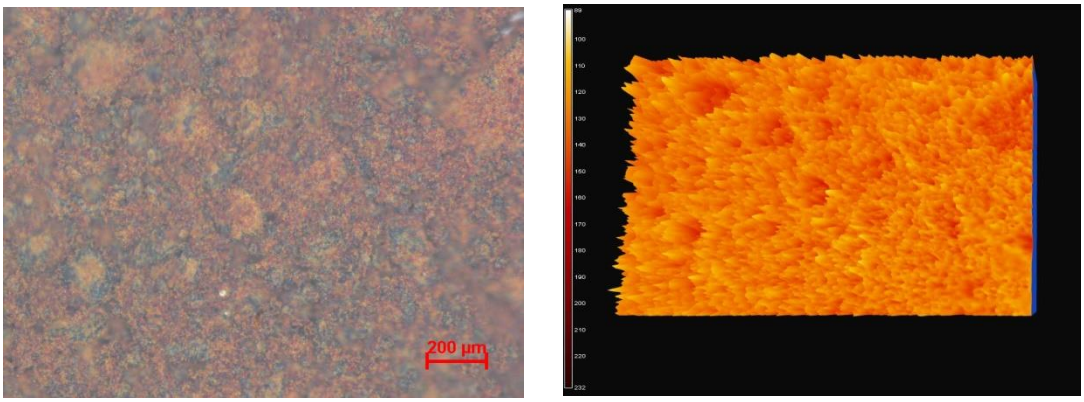

Fig.III.4. *Three-dimensional optical microscopy image of $ZnNiFeCO_3$-LDO recorded at ×50 magnification, showing the surface topography and roughness of the synthesized material.*

Such morphological changes after thermal treatment of LDH precursors have been widely reported and are generally accompanied by the generation of a more defective and irregular surface **[1,2]**.

The presence of surface cavities and interparticle spaces observed in the 3D image may improve the accessibility of adsorption sites and facilitate the diffusion of Congo Red molecules toward the adsorbent surface. However, optical microscopy alone cannot provide a

quantitative determination of pore size distribution or specific surface area; therefore, complementary techniques such as nitrogen adsorption–desorption analysis (BET/BJH method) are required for an accurate evaluation of the textural properties **[14]**.

Overall, the rough surface texture of $ZnNiFeCO_3$-LDO, together with its mixed spinel structure confirmed by XRD, nanoscale crystallite size, and suitable surface charge characteristics (**pH_pzc = 6.9**), is expected to contribute to its favorable adsorption performance toward the removal of Congo Red from aqueous solutions.

III.5 Fourier Transform Infrared Spectroscopy (FTIR) Analysis

The FTIR spectrum of the synthesized $ZnNiFeCO_3$-LDO material is presented in **Figure III.5**. The spectrum exhibits several characteristic absorption bands associated with surface hydroxyl groups, residual carbonate species, and metal–oxygen vibrations characteristic of the mixed oxide structure.

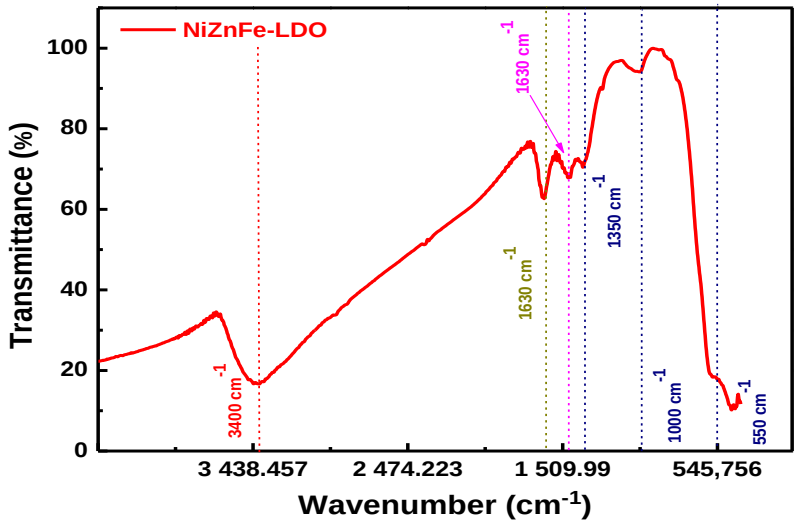

Fig.III.5. *FTIR spectra of $ZnNiFeCO_3$-LDO calcined at 550 °C with assigned vibrational bands, including surface hydroxyl groups (O–H), adsorbed water (H–O–H), residual carbonate species (CO_3^{2-}), C–O / M–OH vibrations, and metal–oxygen (Zn–O, Ni–O, Fe–O) lattice vibrations confirming the formation of a mixed oxide (LDO) structure.*

A broad absorption band centered around **~3400 cm^{-1}** is attributed to the stretching vibration of hydroxyl groups (**O–H**) originating from surface hydroxyl species and physically adsorbed water molecules. The weak absorption band observed around **~1630 cm^{-1}** corresponds to the bending vibration of **H–O–H** groups, confirming the presence of Physisorbed water on the surface of the material **[1, 2]**.

The absorption bands located in the range of **1500–1350 cm⁻¹** are assigned to the asymmetric stretching vibration (ν_3) of carbonate ions (**CO_3^{2-}**). The persistence of these bands after calcination indicates either incomplete decomposition of interlayer carbonate species or re-adsorption of atmospheric CO_2 due to the strong basic character and high CO_2 affinity of LDH-derived mixed oxides **[1–15]**. Additional absorption bands between 1000 and 800 cm^{-1} are associated with C–O stretching vibrations and surface M–OH interactions, confirming the existence of residual carbonate-related species and surface hydroxyl groups.

The most intense features are observed in the low-wavenumber region below 700 cm^{-1}, where the bands are assigned to metal–oxygen (Zn–O, Ni–O, Fe–O) and metal–oxygen–metal (**M–O–M**) vibrations, confirming the formation of a Zn–Ni–Fe mixed oxide network. In particular, the absorption bands located between **600 and 450 cm⁻¹** are attributed to tetrahedral and octahedral metal–oxygen vibrations characteristic of spinel-type ferrite structures. The reduction of LDH-related bands after calcination confirms the dehydroxylation and decarbonation processes leading to the transformation of the LDH precursor into a mixed oxide (**LDO**) phase, in agreement with the XRD results **[2–16]**.

Overall, the **FTIR** analysis provides clear evidence of the successful conversion of $ZnNiFeCO_3$-LDH into $ZnNiFeCO_3$-LDO. The formation of a metal–oxygen framework, together with the persistence of surface hydroxyl and carbonate species, may contribute to the surface reactivity and adsorption performance of the material.

Table III.1 : *FTIR Band Assignments and Vibrational Interpretations of the Calcined Zn–Ni–Fe Mixed Double Oxide.*

Wavenumber (cm^{-1})	**Assignment**	**Interpretation**
~3400	O–H stretching vibration	Surface hydroxyl groups and adsorbed H_2O
~1630	H–O–H bending vibration	Adsorbed water molecules
1500–1350	$\nu_3(CO_3^{2-})$ asymmetric stretching	Residual/intercalated carbonate species
1000–800	C–O stretching and surface M–OH vibrations	Residual carbonate and surface groups
600–450	M–O and M–O–M vibrations (Zn–O, Ni–O, Fe–O)	Formation of Zn–Ni–Fe mixed oxide/spinel phase

III.6 Thermal stability and structural evolution of NiZnFe-LDO (DSC/TGA analysis)

The coupled thermogravimetric analysis (TGA) and differential scanning calorimetry (DSC) of the NiZnFe-LDO material provide detailed insight into its thermal stability and successive physicochemical and structural transformations upon heating. The TGA profile reveals a very limited overall mass loss of approximately 0.9% between 300 K and 1200 K, confirming the high thermal stability of the material and the absence of significant decomposition processes. This slight weight variation is mainly attributed to the removal of weakly adsorbed species, including physisorbed water and residual surface hydroxyl groups associated with the layered double oxide (LDO) precursor **[1, 2]**.

The DSC curve exhibits several distinct thermal events. In the low-temperature region (**300-350 K**), a weak endothermic signal is observed, corresponding to the desorption of physically adsorbed water molecules, a typical behavior reported for LDH- and LDO-derived mixed oxides **[1, 2]**.

Figure III.6 presents the DSC (**Fig.III.6a**) and TGA (**Fig.III.6b**) curves of NiZnFe-LDO. Between 400 K and 500 K, a broad endothermic feature accompanied by a slight mass loss is detected. This stage is associated with progressive dehydroxylation of surface groups (–OH) and condensation reactions leading to the formation of metal–oxygen–metal (M–O–M) bonds (M = Ni, Zn, Fe), resulting in a more condensed and stable oxide network **[1, 3]**.

At approximately **600 K**, a pronounced exothermic peak appears without any significant mass variation. This thermal event is attributed to the crystallization and structural ordering of the $NiZnFe_2O_4$ spinel phase from an initially amorphous or poorly crystallized oxide matrix. This solid-state transformation represents the key step toward the formation of the stable cubic spinel structure and is consistent with previous studies on Ni–Zn ferrites derived from LDH/LDO precursors **[4, 5]**.

In the intermediate temperature range (**700–800 K**), the DSC profile remains stable, indicating that the spinel phase is fully formed and thermally stable in this region. Above 850 K, weak but progressive endothermic effects are observed up to approximately 1150 K. These phenomena are likely associated with subtle cation redistributions between tetrahedral (A) and octahedral (B) sites within the spinel lattice, as well as thermally activated redox equilibria involving Fe^{3+}/Fe^{2+} species, which are commonly reported in ferrite systems at elevated temperatures **[17, 18].**

Finally, at around 1200 K, a more pronounced endothermic peak accompanied by a minor mass loss is detected. This behavior suggests the onset of partial structural destabilization of the spinel framework, possibly due to zinc volatilization or advanced reduction processes affecting iron species. However, the overall spinel structure remains largely preserved, confirming the strong thermal robustness of the material.

Overall, the NiZnFe-LDO exhibits excellent thermal stability up to approximately 850 K, while complete crystallization of the $NiZnFe_2O_4$ spinel phase occurs around 600 K. The observed thermal events are predominantly associated with dehydration, dehydroxylation, and structural ordering rather than decomposition, highlighting the suitability of this material for high-temperature applications such as heterogeneous catalysis, magnetic devices, and functional ceramic systems.

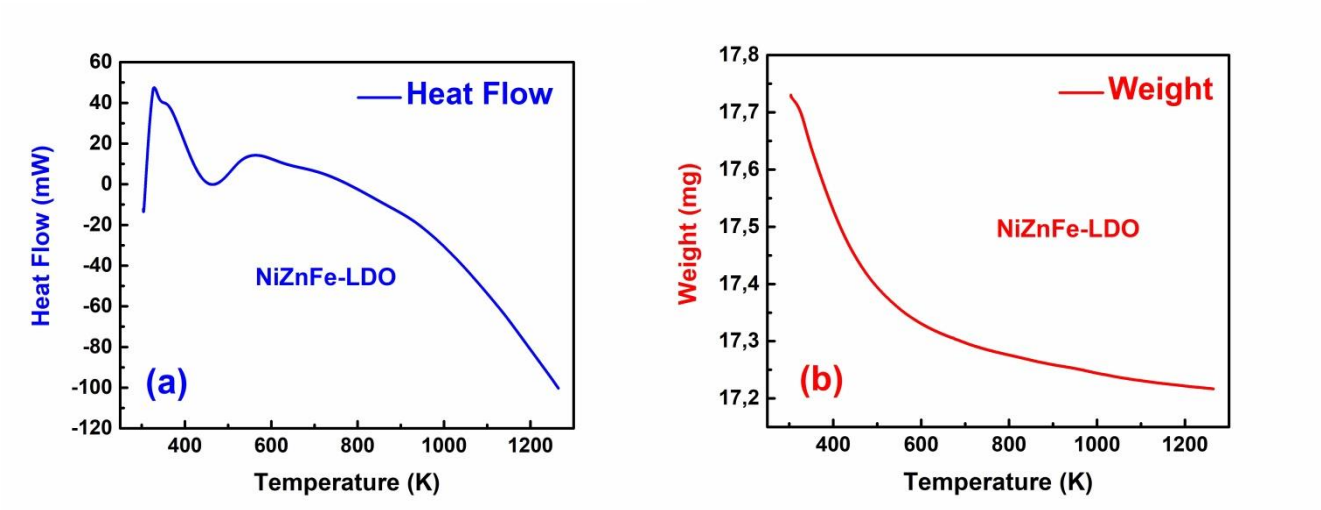

Fig.III.6. *Thermogravimetric and differential scanning calorimetric analysis of NiZnFe-LDO: (a) DSC thermogram; (b) TGA curve.*

IIII Adsorption study

Adsorption experiments were conducted using the synthesized NiZnFe-LDO adsorbent to investigate the adsorption behavior of Congo Red (**CR**), including adsorption kinetics, equilibrium isotherms, and thermodynamic aspects. All experiments were performed in triplicate to ensure reproducibility, and the reported results represent the average values. A stock solution of CR dye (**1000 mg.L^{-1}**) was prepared using deionized water and diluted to the required concentrations for all experiments. The effects of contact time, adsorbent dosage, initial pH, temperature, and initial dye concentration on CR adsorption were systematically investigated.

The adsorption experiments were carried out in 250 mL beakers containing 100 mL of CR solution under continuous magnetic stirring. In a typical experiment, an initial CR concentration of 20 mg.L^{-1} was used and the adsorbent dosage was fixed at 0.5 g.L^{-1} (corresponding to 50 mg of NiZnFe-LDO for 100 mL of solution). The suspension was stirred in the dark for 30 min to ensure adsorption–desorption equilibrium. After adsorption, the solid phase was separated by filtration using a 0.45 μm syringe membrane filter.

The residual concentration of CR was determined using a Rayleigh UV-2601 double-beam UV–Vis spectrophotometer at the maximum absorption wavelength of CR (λmax = 497 nm). The adsorption capacity at equilibrium, Qe (mg.g^{-1}), was calculated using Equation (III.6) **[19]**:

$$\boldsymbol{Q_e = \frac{V}{m}\,(C_0 - C_e)} \qquad (\boldsymbol{III.6})$$

where Q_e (mg.g^{-1}) is the amount of CR adsorbed at equilibrium, C_0 and C_e (mg.L^{-1}) are the initial and equilibrium concentrations of CR, respectively, V (L) is the volume of working solution, and m (g) is the mass of adsorbent (NiZnFe-LDO).

For kinetic studies, batch experiments were performed using 100 mL of CR solution with an initial concentration of 20 mg L^{-1} and 50 mg of NiZnFe-LDO **[20]**. Samples were collected at different time intervals ranging from 0 to 180 min to monitor the adsorption process.

The influence of adsorbent dosage was studied by varying the amount of NiZnFe-LDO at 0.15, 0.25, 0.5, and 0.1 g.L^{-1}. The effect of temperature was investigated at 20, 30, 40, and 50 °C using a thermostatic system. The effect of initial pH on CR adsorption was evaluated by adjusting the solution pH to 2, 3, 4, 5, 9, and 11 using 0.1 M H_2SO_4 or 0.1 M NaOH solutions **[21]**.

For adsorption isotherm studies, batch experiments were carried out using CR solutions with initial concentrations of 20, 30, 40, and 50 mg L^{-1} under identical experimental conditions. The adsorption equilibrium data were analyzed using Langmuir and Freundlich isotherm models, while kinetic data were fitted using pseudo-first-order and pseudo-second-order models. In addition, thermodynamic parameters including Gibbs free energy (ΔG°), enthalpy (ΔH°), and entropy (ΔS°) were evaluated to assess the spontaneity and feasibility of the adsorption process.

IIII.1 Effect of contact time and kinetic modeling

The effect of contact time on the adsorption of Congo Red (CR) by NiZnFe-LDO was investigated under controlled conditions (C_0 = 50 mg.L^{-1}, pH ≈ 7, T = 25 °C). The kinetic behavior of CR adsorption onto NiZnFe-LDO is illustrated in **Figure III.7**.

The adsorption process exhibits a strong dependence on contact time, characterized by a rapid initial uptake followed by a gradual decrease in adsorption rate. During the first 15 min, a fast adsorption was observed, attributed to the abundance of available active sites on the external surface of NiZnFe-LDO. This stage corresponds to a dominant surface adsorption mechanism.

Between 15 and 30 min, the adsorption capacity increased significantly, indicating an enhanced interaction between CR molecules and the active sites of the adsorbent. This behavior reflects a transition stage where both surface adsorption and initial diffusion into internal sites contribute to the overall process.

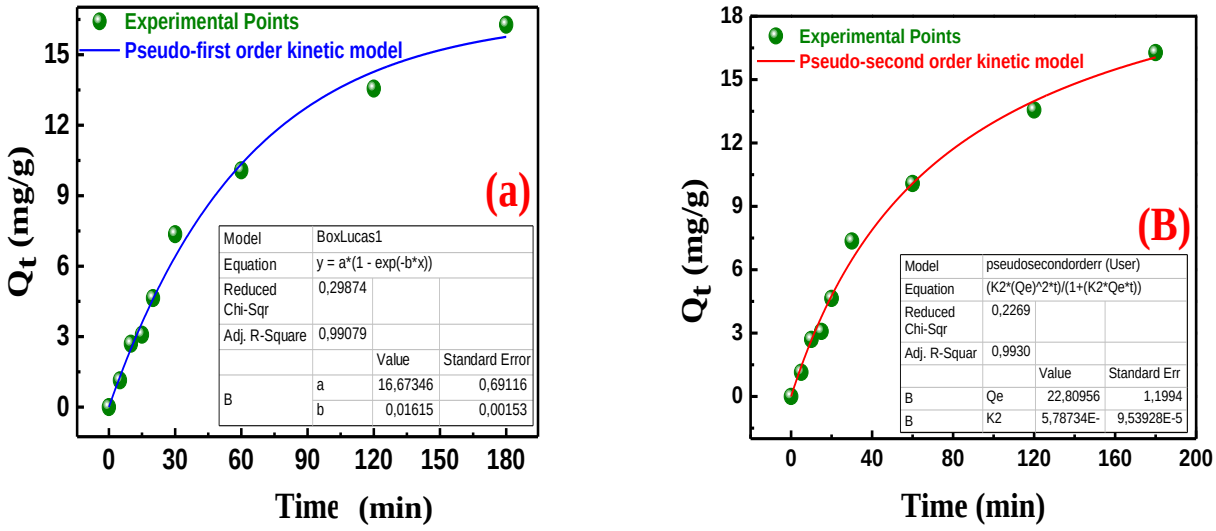

Fig.III.7. *Kinetic modeling of Congo Red adsorption onto NiZnFe-LDO showing (a) pseudo-first-order model and (b) pseudo-second-order mode (adsorbent mass = 50 mg.L^{-1}; C0 = 20 mg.L^{-1}; pH~ 7 ; T= 25 °C).*

After 30 min, the adsorption rate gradually decreased due to progressive occupation of active sites and reduction in available binding sites. The system continued to evolve up to 180 min, indicating that adsorption was still ongoing but at a much slower rate. This suggests that the system approaches a pseudo-equilibrium state without reaching a strict equilibrium within the studied time range, likely due to intraparticle diffusion limitations.

The experimental values of concentration ($\mathbf{C_t}$), adsorption capacity ($\mathbf{Q_t}$), and removal efficiency (**R%**) are summarized in **Table III.2**

Table III.2: *Time-dependent adsorption data for Congo Red removal by NiZnFe-LDO under optimized conditions (C_0 = 50 mg/L, pH ≈ 7, T = 25 °C).*

Time (min)	Abs	C_t (mg.L^{-1})	Q_t (mg.g^{-1})	R (%)
0	1.08	C_0= 20.00	00	0.00
5	1.05	C_5 = 19.43	1.14	2.80
10	1.01	C_{10} = 18.65	2.7	6.75
15	1.00	C_{15} = 18.46	3.08	7.70
20	0.96	C_{20} = 17.68	4.64	11.60
30	0.89	C_{30} = 16.32	7.36	18.40
60	0.82	C_{60} = 14.96	10.08	25.20
120	0.73	C_{120} = 13.22	13.56	33.90
180	0.66	C_{180} = 12.86	16.28	40.70

To elucidate the adsorption mechanism, kinetic data were analyzed using pseudo-first-order (**PFO**) and pseudo-second-order (**PSO**) models. The pseudo-first-order model is expressed as:

$$\boldsymbol{Q_t = Q_e\left(1 - e^{-k_1 t}\right)} \qquad (\boldsymbol{III.7})$$

while the pseudo-second-order model is given by:

$$\boldsymbol{Q_t = \frac{k_2\, Q_e^2\, t}{1 + k_2\, Q_e\, t}} \qquad (\boldsymbol{III.8})$$

The fitting results indicate that both models adequately describe the adsorption behavior of CR onto NiZnFe-LDO. The pseudo-second-order model shows a slightly higher correlation coefficient (R^2 = 0.9930) compared to the pseudo-first-order model (R^2 = 0.99079).

However, the pseudo-first-order model provides a closer agreement between experimental and calculated adsorption capacity (Q_e, exp = 16.28 mg/g vs Q_e, cal = 16.67 mg.g^{-1}), while the pseudo-second-order model overestimates Q_e (22.81 mg.g^{-1}).

Table III.3 : *Kinetics model parameters of CR adsorption over NiZnFe-LDO.*

Pseudo-first order model			
Q_{exp} (mg.g^{-1})	**Q_e (mg.g^{-1})**	**k_1 (g.mg.min^{-1})**	**R^2**
16.28	16,67	0,01615	0,99079
Pseudo-second order model			
Q_{exp} (mg.g^{-1})	**Q_e (mg.g^{-1})**	**k_2 (g.mg.min^{-1})**	**R^2**
16.28	22,80956	0,0005787	0,9930

These results suggest that the adsorption mechanism cannot be attributed exclusively to either physisorption or chemisorption. Instead, it involves a combined mechanism governed by surface interactions and intraparticle diffusion processes within the adsorbent structure.

IIII.2 Effect of adsorbent mass

Figure III.8 illustrates the effect of NiZnFe-LDO dosage on the adsorption capacity (q_e) of Congo Red (**CR**). The results reveal a clear and monotonic decrease in q_e from approximately **139.6** mg.g^{-1} at **0.15** g.L^{-1} to **39.33** mg.g^{-1} at **1.0** g.L^{-1}, demonstrating a well-defined inverse relationship between adsorbent dosage and adsorption capacity per unit mass.

This behavior can be rationalized through several complementary physicochemical mechanisms. At low adsorbent dosages, the number of available active sites is limited relative to the high concentration of **CR** molecules in solution. Under these conditions, each unit mass of **NiZnFe-LDO** is exposed to a large number of dye molecules, ensuring maximum occupancy of adsorption sites and consequently yielding the highest q_e values. This suggests that at low doses, the adsorbent operates near its full adsorption potential, with minimal waste of surface capacity.

As the adsorbent dosage progressively increases, the total number of active sites available in the system exceeds the amount required to adsorb the fixed quantity of CR present in solution. This imbalance between available sites and dye molecules results in a significant underutilization of the adsorbent surface, reflected in the steady decline of q_e. In other words, while the total amount of CR removed from solution may increase or stabilize, the adsorption capacity per gram of adsorbent decreases substantially.

Furthermore, at elevated dosages, interparticle interactions become more pronounced. The tendency of NiZnFe-LDO particles to aggregate at higher concentrations leads to a reduction in the effective surface area exposed to the solution, thereby limiting the accessibility of active sites to CR molecules. This aggregation phenomenon not only diminishes the available surface for adsorption but may also create diffusion barriers that slow the transport of dye molecules to the interior adsorption sites, further reducing the overall efficiency per unit mass **[23].**

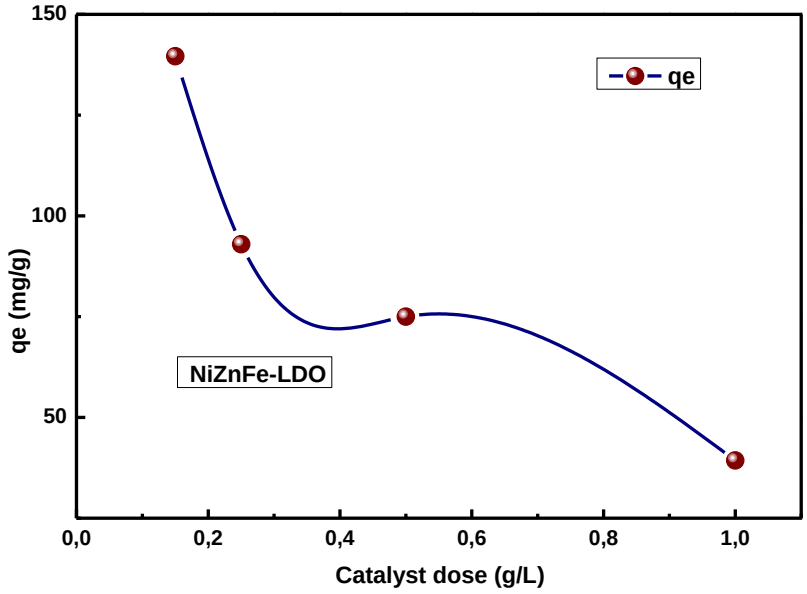

Fig.III.8. *Effect of adsorbent dosage of NiZnFe-LDO on the adsorption capacity of CR (C_0 = 20 mg.L^{-1}, pH ≈ 7, T = 25 °C).*

From a practical standpoint, these findings highlight the importance of optimizing the adsorbent dosage to achieve the best balance between adsorption capacity and removal efficiency. A dosage of **0.15 g.L^{-1}** appears to maximize q_e under the studied conditions, making it the most efficient dose in terms of adsorbent utilization, while higher doses may be considered when total pollutant removal is prioritized over adsorption capacity.

IIII.3 Effect of pH

The effect of solution pH on the adsorption capacity (**q_e**) of Congo Red (CR) onto NiZnFe-LDO presented in **Figure III.9** The adsorption capacity increased from approximately **6.8** mg g^{-1} at pH **2** to about **9.8** mg g^{-1} at pH **3**, after which it remained nearly constant between pH 3 and 9. This behaviour indicates that the adsorption process is effective

over a wide pH range, suggesting a strong affinity between CR molecules and the active sites of the adsorbent.

The relatively lower adsorption capacity observed at pH 2 may be attributed to the modification of the adsorbent surface under strongly acidic conditions, which may reduce the accessibility of active sites and consequently limit the interaction between CR molecules and the NiZnFe-LDO surface. In contrast, the sharp decrease in adsorption capacity observed at pH 11 indicates that strongly alkaline conditions are unfavorable for adsorption. This decline may result from the abundance of OH^- ions, which compete with CR molecules for adsorption sites and reduce the electrostatic interactions between the dye and the adsorbent surface **[24]**.

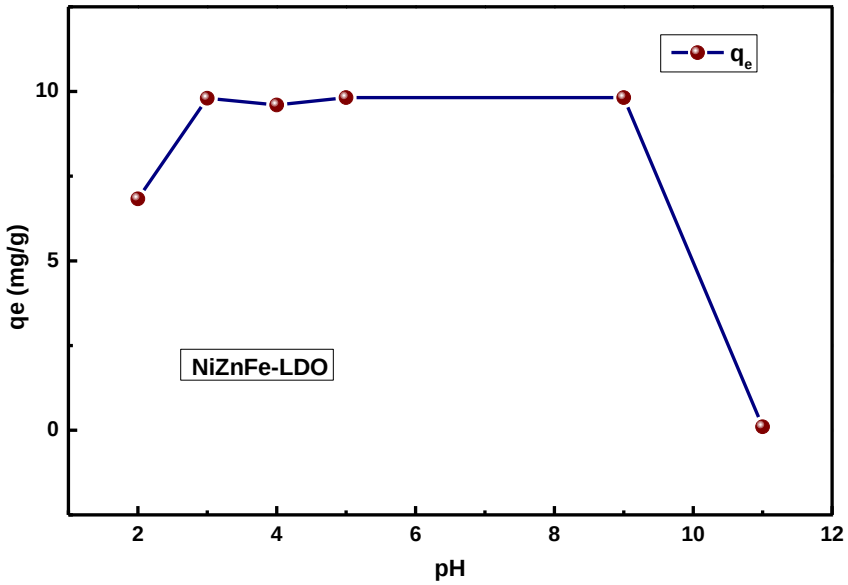

Fig.III.9*. Effect of solution pH on the adsorption capacity (q_e) of CR onto NiZnFe-LDO (adsorbent dosage = 0.5 g.L^{-1}; C_0 = 20 mg.L^{-1}; T = 25 °C).*

IIII.4 Effect of the initial concentration

Figure III.10 illustrates the effect of initial **CR** concentration on the adsorption capacity (**q_e**) of NiZnFe-LDO. The results show a significant increase in **q_e** from **3.58** mg.g^{-1} at **20** ppm to **67.42** mg.g^{-1} at **50** ppm, reflecting a strong dependence of the adsorption process on the initial dye concentration.

At low concentrations (**20–30 ppm**), the relatively limited number of CR molecules in solution compared to the abundance of available active sites on the NiZnFe-LDO surface

results in modest q_e values. As the concentration increases from 30 to 40 ppm, a sharp rise in adsorption capacity is observed **(+40 mg.g^{-1})**, which can be attributed to the enhanced concentration gradient acting as a driving force for mass transfer, promoting the diffusion of CR molecules toward the adsorbent surface and facilitating their interaction with active adsorption sites.

Beyond 40 ppm, the rate of increase in q_e slows considerably, with only a marginal gain of approximately **4 mg.g^{-1}** between 40 and 50 ppm. This behavior indicates the progressive saturation of available adsorption sites, as the surface of NiZnFe-LDO becomes increasingly occupied by CR molecules. The adsorption capacity thus approaches a maximum plateau value of approximately **67.42 mg.g^{-1}**, suggesting that the adsorbent has reached near-complete site occupancy under the studied conditions.

This trend, characterized by an initial increase followed by a progressive approach to saturation, suggests the gradual occupation of available adsorption sites on the NiZnFe-LDO surface. However, a detailed determination of the adsorption mechanism and surface heterogeneity requires adsorption isotherm modeling (e.g., Langmuir and Freundlich models). These results confirm the high affinity of NiZnFe-LDO toward CR molecules and demonstrate its effectiveness as an adsorbent for dye removal from aqueous solution **[25]**.

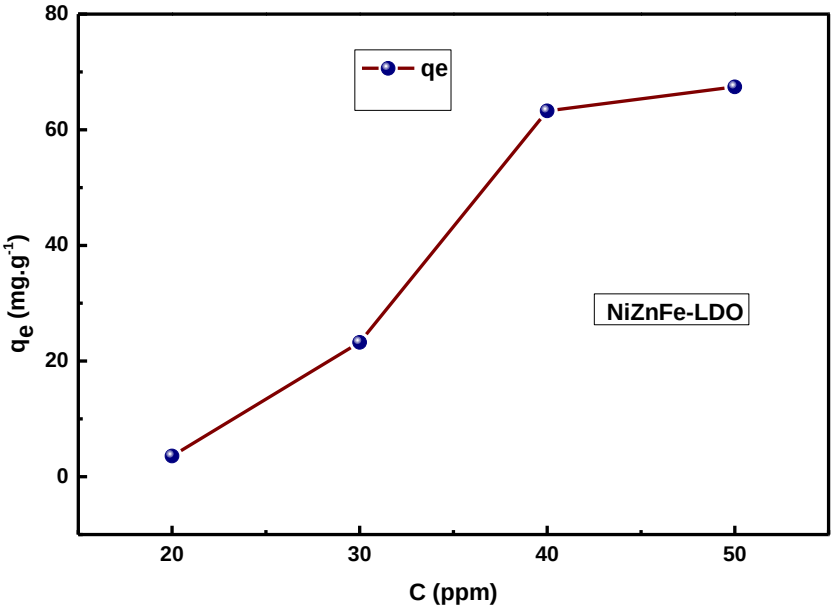

Fig.III.10. *Effect of initial concentration on the adsorption capacity (adsorbent mass = 20 mg.L^{-1}; pH~ 3 ; T= 25 °C).*

IIII.5 Effect of the temperature

The thermodynamic parameters of the adsorption process were evaluated using the distribution coefficient (**K_d**), Gibbs free energy change (**ΔG°**), enthalpy change (**ΔH°**), and entropy change (**ΔS°**). These parameters were determined over the temperature range 293–323 K (**20–50 °C**) using the Van't Hoff approach, according to the following equations :

$$\Delta G^\circ = -RTlnKd \qquad (\mathbf{III.6})$$

$$lnKd = -\Delta H^\circ/R \cdot 1/T + \Delta S^\circ/R \qquad (\mathbf{III.7})$$

where R is the universal gas constant (**8.314 J.mol^{-1}.K^{-1}**) and T is the absolute temperature in Kelvin. The values of **ΔH°** and **ΔS°** were extracted from the slope and intercept of the linear plot of **ln(K_d)** versus **1/T**, which yielded a high correlation coefficient of **R^2 = 0.987**, confirming the validity and reliability of the Van't Hoff model for this adsorption system.

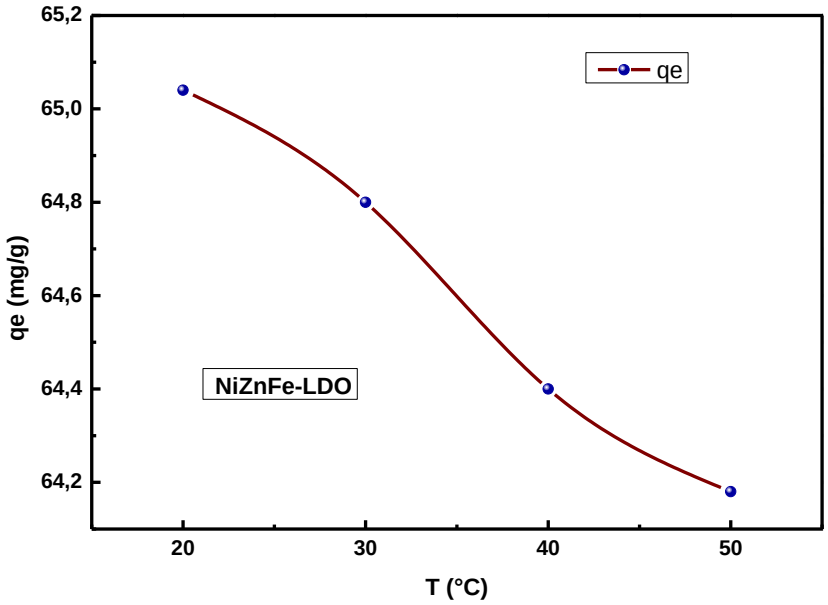

Fig.III.11. *Effect of temperature on the adsorption capacity.*

Fig.III.11 illustrates the variation of the equilibrium adsorption capacity (**q_e**) of Congo Red onto NiZnFe-LDO as a function of temperature over the range 20–50 °C. The results reveal a slight but consistent decrease in **q_e** from **65.04** mg.g^{-1} at 20 °C to **64.18** mg.g^{-1} at 50 °C, indicating that elevated temperatures are unfavorable for CR adsorption onto NiZnFe-LDO.

This behavior is consistent with the exothermic nature of the adsorption process, as confirmed by the negative value of ΔH° (−0.363 kJ.mol^{-1}). According to Le Chatelier's principle, increasing the temperature shifts the adsorption equilibrium toward desorption,

thereby reducing the amount of dye retained on the adsorbent surface. The low absolute value of ΔH° further suggests that the process is governed by weak physical interactions — including van der Waals forces, electrostatic attractions, and hydrogen bonding — rather than strong chemical bonds, classifying the adsorption as predominantly physisorption in nature **[25].**

Furthermore, the slight decrease in the distribution coefficient (Kd) with increasing temperature, from 65.04 at 293 K to 64.18 at 323 K, corroborates this interpretation, as elevated thermal energy progressively weakens the physical interactions between CR molecules and the active surface sites of NiZnFe-LDO. From a practical perspective, these findings indicate that ambient temperature (293.15– 298.15 K) represents the optimal operating condition for CR removal, which is advantageous for real-scale wastewater treatment applications as no external heating is required.

The negative values of **ΔG°** at all studied temperatures, ranging from **−10.18 kJ.mol^{-1}** at 293 K to **−11.18 kJ.mol^{-1}** at 323K; confirm the spontaneous and thermodynamically favorable nature of CR adsorption onto NiZnFe-LDO under all tested conditions. The gradual increase in the magnitude of ΔG° with increasing temperature suggests that the spontaneity of the process is marginally enhanced at higher temperatures, which may be attributed to the growing contribution of the entropic term (**TΔS°**) at elevated thermal conditions.

The negative value of ΔH° (**−0.363 kJ.mol^{-1}**) confirms the exothermic nature of the adsorption process. The low absolute value of ΔH° suggests that physical interactions, including van der Waals forces, hydrogen bonding, and electrostatic attractions, play a significant role in the adsorption of CR onto NiZnFe-LDO. This result indicates that the adsorption process is mainly governed by weak interactions rather than strong chemical bonding. The exothermic character is further corroborated by the slight but consistent decrease in $\mathbf{K_d}$ with increasing temperature, as elevated thermal energy progressively weakens the physical interactions between the adsorbate and the adsorbent surface.

The positive value of ΔS° (**+33.47 J.mol^{-1}K^{-1}**) reflects an increase in randomness and disorder at the solid–liquid interface during the adsorption process. This behavior is attributed to the displacement and release of water molecules previously coordinated to the CR molecules and to the surface hydroxyl groups of NiZnFe-LDO, which increases the translational entropy of the system. Additionally, the structural rearrangements occurring at the adsorbent surface upon CR binding may contribute to the overall increase in interfacial disorder.

The calculated thermodynamic parameters are summarized in **Table III.4**.

Table III.4 : *Thermodynamic parameters for CR adsorption onto NiZnFe-LDO at different temperatures.*

T (°C)	T (K)	K_d	ln(K_d)	ΔG° (kJ.mol^{-1})
20	293.15	65.04	4.1750	−10.18
30	303.15	64.80	4.1713	−10.51
40	313.15	64.40	4.1651	−10.84
50	323.15	64.18	4.1617	−11.18
		ΔH°	**−0.363 kJ.mol^{-1}**	
		ΔS°	**+33.47 J.mol.K^{-1}**	
		R^2	**0.987**	

Collectively, the thermodynamic analysis confirms that the adsorption of CR onto NiZnFe-LDO is a spontaneous and exothermic process, mainly governed by physical interactions and accompanied by an increase in interfacial disorder.

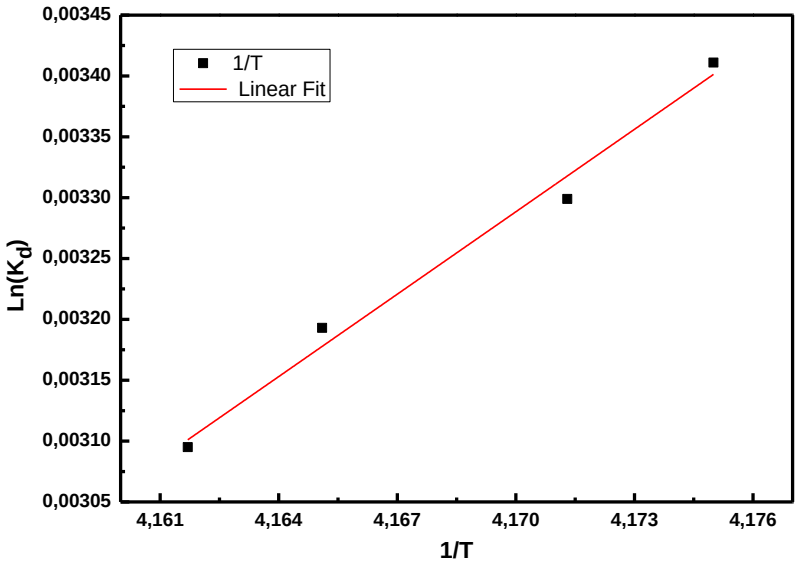

Fig.III.12. *Van't Hoff plot for the adsorption of CR onto NiZnFe-LDO.*

These results highlight the thermodynamic feasibility of the adsorption process across the entire studied temperature range and support the potential of NiZnFe-LDO as an efficient and thermodynamically favorable adsorbent for the removal of CR from aqueous solutions **[25].**

IIII.6 Mechanism of adsorption on NiZnFe-LDO

To elucidate the adsorption mechanism of Congo Red (CR) dye on NiZnFe-LDO, both surface chemistry and structural transformation phenomena must be considered. The

adsorption process is mainly governed by surface interactions in combination with possible reconstruction behavior in aqueous medium.

NiZnFe-LDO, obtained by calcination of layered double hydroxide precursors, consists of mixed metal oxides with abundant surface metal–oxygen (**M–O**) sites. When placed in aqueous dye solution, the material exhibits high affinity toward anionic Congo Red molecules. The adsorption process is primarily driven by electrostatic attraction between negatively charged dye species (**$–SO_3^-$** groups of **CR**) and positively polarized surface sites, as well as surface complexation involving metal centers (**Ni^{2+}, Zn^{2+}, Fe^{3+}**).

In addition, upon contact with water, the NiZnFe-LDO surface undergoes partial hydration, leading to the formation of hydroxylated species (**M–OH**).

These newly generated active sites further enhance dye adsorption through hydrogen bonding and ligand-like interactions. Furthermore, the material may exhibit a partial "memory effect", where the mixed metal oxide structure tends to reconstruct into a layered double hydroxide-like phase in aqueous media. This reconstruction can contribute to dye uptake by increasing surface ordering and providing additional adsorption sites. However, in the case of Congo Red adsorption, the dominant mechanism remains surface adsorption rather than complete intercalation.

The overall mechanism is schematically illustrated in **Figure III.13**. Schematic representation of the proposed mechanism of Congo Red adsorption on NiZnFe-LDO involving surface complexation, electrostatic interactions, and partial hydration-induced reconstruction (memory effect).

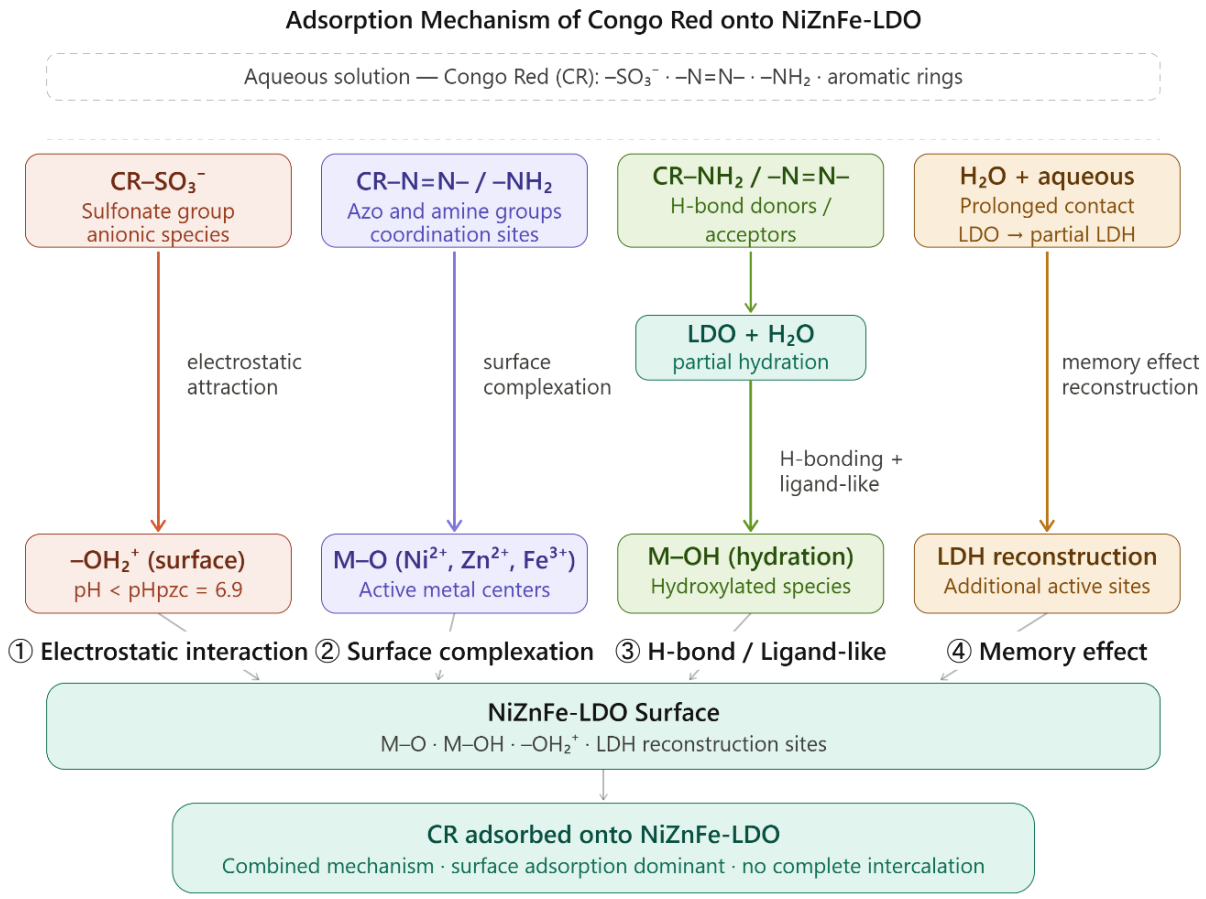

Fig.III.13. *Schematic representation of the proposed adsorption mechanism of Congo Red onto NiZnFe-LDO, involving four pathways: electrostatic interaction, surface complexation, hydrogen bonding / ligand-like interactions via M–OH species, and partial LDH reconstruction (memory effect) (AI generated).*

Therefore, the adsorption mechanism of NiZnFe-LDO can be described as a combined process involving :

- electrostatic interaction between dye molecules and surface sites,
- surface complexation with metal–oxygen centers, and
- partial hydration-induced reconstruction (memory effect), which enhances adsorption performance.

Overall, the calcination-derived LDO structure provides a highly reactive surface, making it an efficient adsorbent for Congo Red removal through mainly surface-controlled adsorption processes.

V Conclusion

The present chapter demonstrated the successful synthesis and characterization of NiZnFe-LDO as an efficient adsorbent for Congo Red removal from aqueous solution. XRD confirmed the formation of a nanocrystalline cubic spinel phase (crystallite size ≈ 11.5 nm), while TGA/DSC revealed excellent thermal stability up to 850 K. The determined pH_{PZC} of 6.9 confirmed favorable surface charge conditions for the adsorption of anionic CR molecules.

Adsorption experiments showed that the process follows pseudo-first-order kinetics, is effective over a wide pH range (3–9), and reaches a maximum adsorption capacity of 67.42 $mg.g^{-1}$ at 50 ppm. Thermodynamic analysis confirmed that the adsorption is spontaneous, exothermic, and physisorption-dominated, with ambient temperature identified as the optimal operating condition.

The proposed mechanism involves a combination of electrostatic interactions, surface complexation, hydrogen bonding via M–OH species, and partial LDH reconstruction (memory effect), with surface adsorption as the dominant pathway. Collectively, these findings establish NiZnFe-LDO as a promising and thermodynamically favorable adsorbent for the treatment of dye-contaminated wastewater.

References

[1]- Cavani, F., Trifirò, F., Vaccari, A. (1991). Hydrotalcite-type anionic clays: Preparation, properties and applications. Catalysis Today, 11, 173–301.

[2]- Rives, V. (2020). Layered Double Hydroxides: Present and Future. Springer

[3] - He, J., et al. (2021). Thermal decomposition and structural evolution of LDH-derived mixed oxides. Applied Clay Science, 202.

[4]- Wang, Q., et al. (2022). Structural evolution of LDH materials and derived oxides. Journal of Colloid and Interface Science, 606, 1–15.

[5]- Zhao, Y., et al. (2023). Thermal transformation of LDH to spinel oxides. Materials Chemistry and Physics, 295, 127–138.

[6]- Kim, J. S., et al. (2003). Crystallization behavior of NiZn ferrite from LDH precursors. Journal of Materials Science, 38, 4325–4330.

[7]- Valenzuela, R. (2012). Magnetic Ceramics. Cambridge University Press.

[8]- Zhang, L., et al. (2021). Cation distribution in Ni–Zn ferrite spinels. Ceramics International, 47, 11200–11210.

[9]- Kosmulski, M. (2016). Ionic Equilibria in Natural Waters. CRC Press.

[10]- Kosmulski, M. (2009). Surface charge properties of metal oxides. Journal of Colloid and Interface Science, 337, 439–448.

[11]- Gupta, V. K., Suhas (2009). Application of low-cost adsorbents for dye removal. Journal of Environmental Management, 90, 2313–2342.

[12]- Foo, K. Y., Hameed, B. H. (2010). Insights into the modeling of adsorption isotherm systems. Chemical Engineering Journal, 156, 2–10.

[13]- Crini, G. (2006). Non-conventional low-cost adsorbents for dye removal. Bioresource Technology, 97, 1061–1085.

[14]- Thommes, M., Kaneko, K., Neimark, A. V., Olivier, J. P., Rodriguez-Reinoso, F., Rouquerol, J., & Sing, K. S. W. (2015). Physisorption of gases, with special reference to the evaluation of surface area and pore size distribution (IUPAC Technical Report). Pure and Applied Chemistry, **87**, 1051–1069.

[15]- He, J., Wei, M., Li, B., Kang, Y., Evans, D. G., & Duan, X. (2006). Preparation of layered double hydroxides and their applications as additives in polymers: A review. **Applied Clay Science**, 32, 1–13.

[16]- Waldron, R. D. (1955). Infrared spectra of ferrites. **Physical Review**, 99, 1727–1735.

[17]- Gadalla, A. M., Yu, H. F. (1990). High-temperature transformations in ferrites. Thermochimica Acta, 164, 21–36.

[18]- Smit, J., Wijn, H. P. J. (1959). Ferrites. Philips Technical Library.

[19]- Chen, T., Da, T., & Ma, Y. (2021). Reasonable calculation of the thermodynamic parameters from adsorption equilibrium constant. Journal of Molecular Liquids, 322, 114980.

[20]- Arroussi, A., Laksaci, H., Mokri, H., & Boukli-Hacene, L. (2025). Synthesis and characterization of Ni based metal organic framework for enhancing the removal of typical organic dyes. Journal of Macromolecular Science, Part B, 64(7), 785-800.

[21]- Bahman, H., Gharanjig, K., Ghasemi, E., Kazemian, H., & Hosseinnezhad, M. (2026). Comparative synthesis of quercetin-loaded Zn/Al LDH via co-precipitation and ion exchange: RSM optimization, adsorption behavior, and antioxidant activity. Journal of Molecular Liquids, 129724.

[22]- Harja, M., Buema, G., & Bucur, D. (2022). Recent advances in removal of Congo Red dye by adsorption using an industrial waste. *Scientific Reports*, *12*(1), 6087.

[23]- Rasheed, A. A., Muhammad, H. S., Jakada, Y., & Salahudeen, N. (2025). Effect of Adsorbent Dosage on the Kinetics and Isotherms of Lead (II) Removal from Aqueous Solution Using Corn Husk. ARID ZONE JOURNAL OF ENGINEERING, TECHNOLOGY AND ENVIRONMENT, 21(3), 702-718

[24]- Nguyen, T. H. T., Dao, T. T. U., Pham, G. V., Do, T. S., Nguyen, T. T. L., Nguyen, T. H. L., ... & Tien, N. A. (2020, January). Effect of pH on the adsorption behaviour of Congo Red Dye on the Mg-Al layered double hydroxide. In IOP Conference Series: Materials Science and Engineering (Vol. 736, No. 2, p. 022077). IOP Publishing.

General Conclusion

General Conclusion

The present work focused on the synthesis, characterization, and application of NiZnFe-layered double oxide (NiZnFe-LDO) for the removal of organic pollutants from aqueous media, with particular emphasis on the anionic dye Congo Red (CR). This study was motivated by the growing concern over water contamination by refractory organic pollutants and the recognized limitations of conventional treatment processes in achieving complete and cost-effective dye removal.

NiZnFe-LDO was successfully prepared via the co-precipitation method followed by calcination of the NiZnFe-LDH precursor at 550 °C. Comprehensive physicochemical characterization (XRD, FTIR, 3D optical microscopy, STA/DSC-TGA, and UV–Vis spectroscopy) confirmed the formation of a nanocrystalline cubic spinel phase (crystallite size ≈ 11.5 nm, lattice parameter ≈ 8.36 Å) with excellent thermal stability up to 850 K and a pHPZC of 6.9.

The adsorption performance of NiZnFe-LDO toward CR was systematically evaluated, yielding a maximum adsorption capacity of 67.42 $mg.g^{-1}$. The process followed pseudo-first-order kinetics, remained effective over a broad pH range (3–9), and was confirmed to be spontaneous ($\Delta G° = -10.18$ to -11.18 $kJ.mol^{-1}$), exothermic ($\Delta H° = -0.363$ $kJ.mol^{-1}$), and governed by physisorption through a combined mechanism involving electrostatic interactions, surface complexation, hydrogen bonding via M–OH species, and partial LDH reconstruction (memory effect).

Based on these encouraging results, future work should focus on optimizing the synthesis parameters of NiZnFe-LDO to further enhance both its adsorption capacity and photocatalytic activity, while maintaining a simple, cost-effective, and environmentally friendly preparation route.

Abstract

In this work we present the synthesis, characterization, and application of NiZnFe-Layered double oxide (NiZnFe-LDO), the catalyst was synthesized via the co-precipitation method, and was subsequently characterized using various analytical techniques to investigate its structural, morphological, optical, and physicochemical properties. As an excellent adsorbent and photocatalyst for the removal of different organic contaminants from aqueous media, particularly the anionic Congo Red (CR) dye.

The adsorption and photocatalytic efficiencies of the synthesized material were evaluated under various operating conditions to determine its suitability for wastewater treatment applications.

Keywords: Emergent contaminants (ECs), Advanced oxidation processes (AOPs), Layered double hydroxides (LDHs), Layered double oxides (LDOs), adsorption, Congo Red (CR).

Résumé

Dans ce travail, nous présentons la synthèse, la caractérisation et l'application de l'oxyde double en couches NiZnFe-LDO. Ce catalyseur a été synthétisé par la méthode de co-précipitation, puis caractérisé à l'aide de diverses techniques analytiques afin d'étudier ses propriétés structurelles, morphologiques, optiques et physicochimiques. Il s'agit d'un excellent adsorbant et photocatalyseur pour l'élimination de différents contaminants organiques des milieux aqueux, en particulier le colorant anionique rouge Congo (CR).

Les efficacités d'adsorption et de photocatalyse du matériau synthétisé ont été évaluées dans diverses conditions de fonctionnement afin de déterminer son adéquation aux applications de traitement des eaux usées.

Mots-clés : Contaminants émergents (CE), Procédés d'oxydation avancés (POA), Hydroxydes doubles en couches (LDH), Oxydes doubles en couches (LDO), adsorption, Rouge Congo (CR).

الملخص

في هذا العمل، نقدم تخليق وتوصيف وتطبيق أكسيد الهيدروكسيد المزدوج الطبقات القائم على النيكل والزنك والحديد (NiZnFe-LDO).تم تحضير هذا المحفز باستعمال طريقة الترسيب المشترك، ثم تم توصيفه باستخدام مجموعة من التقنيات التحليلية المختلفة لدراسة خصائصه البنيوية والمورفولوجية والبصرية والفيزيائية الكيميائية .أظهر المركب المحضر كفاءة عالية بوصفه مادة ممتازة ومحفزًا ضوئيًا لإزالة مختلف الملوثات العضوية من الأوساط المائية، مع التركيز بشكل خاص على صبغة الكونغو الأحمر الأنيونية (Congo Red, CR)

تم تقييم كفاءة الامتزاز والتحفيز الضوئي للمادة المحضرة تحت ظروف تشغيل مختلفة بهدف تحديد مدى ملاءمتها لتطبيقات معالجة مياه الصرف الصحي وإزالة الملوثات العضوية من المحاليل المائية.

الكلمات المفتاحية :الملوثات الناشئة(ECs) ، عمليات الأكسدة المتقدمة(AOPs) ، الهيدروكسيدات المزدوجة الطبقات (LDHs)، الأكاسيد المزدوجة الطبقات (LDOs)، الادمصاص، الكونغو الأحمر(CR) .